Phase-field-based simulation of axisymmetric binary fluids by using vorticity-streamfunction formulation

Jun-Jie Huang*

Department of Engineering Mechanics,
Chongqing University,
Chongqing 400044, China
and
Chongqing Key Laboratory of
Heterogeneous Material Mechanics
(Chongqing University),
Chongqing 400044, China
and
State Key Laboratory of Mechanical Transmission,
Chongqing University,
Chongqing 400044, China
Email: jjhuang1980@gmail.com
Email: jjhuang@cqu.edu.cn
*Corresponding author

Haibo Huang

Department of Modern Mechanics,
University of Science and Technology of China,
Hefei, Anhui 230026, China
Email: huanghb@ustc.edu.cn

Shi-Long Wang

State Key Laboratory of Mechanical Transmission,
Chongqing University,
Chongqing 400044, China
Email: slwang@cqu.edu.cn

Abstract: We propose a numerical method for the simulation of axisymmetric binary fluids based on the phase-field theory and vorticity-streamfunction formulation. Unlike most existing methods that solve the incompressible Navier-Stokes equations in the velocity-pressure form, we recast the equations into the vorticity-streamfunction form, which only need to treat one evolution equation of the vorticity for two-dimensional (2-D) or axisymmetric (pseudo 2-D) problems. Besides, this formulation enforces the continuity equation more easily. This method is verified through a series of benchmark problems under axisymmetric conditions, including the Laplace relation for a quiescent drop, coalescence of two drops, and the contact angle of a drop on a smooth wall with given wettability. Good agreements with theoretical relations or another numerical method are achieved for all these problems.

Keywords: numerical simulation; axisymmetric two phase flow; phase field; vorticity streamfunction; drop dynamics.

Biographical notes: Jun-Jie Huang is an Associate Professor at the Department of Engineering Mechanics, Chongqing University. He received his PhD from the National University of Singapore.

Haibo Huang is an Associate Professor at the Department of Modern Mechanics, University of Science and Technology of China. He received his PhD from the National University of Singapore.

Shi-Long Wang is a Professor at the State Key Laboratory of Mechanical Transmission, Chongqing University. He received his PhD from Chongqing University.

1 Introduction

Multiphase flows are important in both many natural phenomena and many industries (e.g., oil and gas, and chemical engineering). They are found in some emerging technologies as well, for instance, digitial microfluidics (Stone et al., 2004). Mathematical modelling and computer simulation of complex multiphase flows have experienced substantial development in the past two decades. The most famous continuum-based simulation methods include the methods of front-tracking (FT) (Unverdi and Tryggvason, 1992), volume-of-fluid (VOF) (Scardovelli and Zaleski, 1999), level-set (LS) (Chang et al., 1996), and phase-field (PF) (also known as diffuse-interface) (Anderson et al., 1998; Jacqmin, 1999). For all these methods, two fundamental requirements are imposed on them: first, to capture or track the interface motion; second, to capture the flow with the interfacial tension effect. Correspondingly, two sets of equations must be solved, one for the interface dynamics and the other for the fluid flow. When incompressible flow is considered, the latter includes the incompressible Navier-Stokes equations (NSEs) with interfacial tension force. The methods mentioned above (FT, VOF, LS and PF) differ from each other mainly in the way to capture/track the interface dynamics and that to model the interfacial tension effect (for near-wall flows, the ways to treat the contact angle and contact line also differ). The flow governing equations solved in all methods share a common form, and they are consisted of the continuity and momentum equations. Most existing works adopt the flow equations in the velocity-pressure (VP) form which is relatively straightforward. In the literature, an alternative formulation using the vorticity and streamfunction has also been developed for incompressible flow, in particular for 2-D or pseudo 2-D problems. There have been quite some efforts devoted to solving the equations in the vorticity-streamfunction (VS) formulation (E and Liu, 1996; Chen et al., 2008b) partly because it only requires to solve one evolution equation for the vorticity and the continuity condition is automatically satisfied in this formulation through the definition of the streamfunction. This formulation also allows the direct monitoring of the vorticity, an important physical quantity in fluid dynamics. At the same time, it is acknowledged that this formulation has certain limitations as compared with the VP formulation. The most noticeable one is that it is limited to (pseudo) 2-D problems. Besides, the boundary conditions (BCs) for the main variables are a major issue as BCs are commonly given in terms of the velocity and pressure. Fortunately, in the literature some workable solutions have been provided (e.g., see E and Liu, 1996).

As far as we know, till now for incompressible multiphase flow simulation, only a few works employed the VS formulation in practice. Chang et al. (1996) developed a LS formulation for two-phase flows using both the VP and VS formulations for incompressible flow (this appears to be the only LS work that used the VS formulation). Anderson et al. (2006) studied the bulk behaviour of polymer blends in sliding bi-period frames using the simplified equations in VS formulation and the PF model for immiscible fluids. Acar (2009) also carried out a series of simulations of interface dynamics using a set of equations on similar basis. However, the unsteady and convective terms were neglected in both works, which made it possible to obtain the biharmonic equation for the streamfunction. Besides, only 2-D problems were considered in all of the above works.

Axisymmetric flows are special cases of three-dimensional (3-D) flows. The axisymmetric conditions make them much simplified and two spatial coordinates are sufficient to describe them. Because of the effective reduction of dimension, the use of an axisymmetric simulation can significantly save the computational cost as compared with a fully 3-D simulation. Thus, axisymmetric simulation has always been pursued and employed whenever applicable. However, all existing axisymmetric simulations of multiphase flows employ the VP formulation. This situation is partly due to the rare use of the VS formulation. To the best of our knowledge, the present work is the first to develop a complete numerical method for axisymmetric multiphase flows using the VS formulation. We note that the PF model is not the only choice for interface dynamics and other methods like VOF and LS may also be employed together with the VS formulation. If another method (VOF, LS or some others) is used, the interfacial tension terms need be modified accordingly, but the main framework and elements given here are still useful.

The paper is organised as follows. Section 2 presents the PF model and the numerical method. Section 3 illustrates the application of the proposed method to a few specific problems, together with discussions on some important issues including mass conservation and convergence. Section 4 concludes this paper.

2 Theoretical model and numerical methodology

In the present method, interface dynamics and interfacial tension effects are taken into account through the PF model for binary fluids whereas the incompressible flow is described by the continuity and momentum equations in the VS formulation. The two types of dynamics are closely coupled with each other. The individual components are described as follows.

2.1 Phase-field model and interface dynamics

In the PF model for binary fluids, different fluids are distinguished by an order parameter ϕ. For the system a free energy functional is defined as (Badalassi et al., 2003; Briant and Yeomans, 2004; Huang et al., 2009),

$$
\mathcal{F}(\phi, \boldsymbol{\nabla}\phi) = \int_V \left(\Psi(\phi) + \frac{1}{2}\kappa|\boldsymbol{\nabla}\phi|^2 \right) dV + \int_S \varphi(\phi_S) dS, \tag{1}
$$

where $\Psi(\phi)$ is the *bulk free energy* density taking the *double-well* form,

$$
\Psi(\phi) = a(\phi^2 - 1)^2, \tag{2}
$$

with a being a constant. This form indicates that ϕ varies between -1 (in one fluid) and 1 (in the other fluid). The second term is the *interfacial energy* density with κ being another constant. The last term in the surface integral is the *surface energy* density with ϕ_S being the order parameter on the surface. In this work, we use the following surface energy (Jacqmin, 2000; Villanueva and Amberg, 2006; Yue et al., 2010),

$$
\varphi(\phi_S) = -\sigma\cos\theta_w \frac{\phi_S(3 - \phi_S^2)}{4} + \frac{1}{2}(\sigma_{w1} + \sigma_{w2}), \tag{3}
$$

where $\varphi(\pm 1)$ gives the fluid-solid interfacial tensions σ_{w1} and σ_{w2} between the wall and fluid 1 (with $\phi = 1$) and fluid 2 (with $\phi = -1$), respectively. Young's equation determines θ_w as,

$$
\cos\theta_w = \frac{\sigma_{w2} - \sigma_{w1}}{\sigma}. \tag{4}
$$

The coefficients a and κ can be related to the interfacial tension σ and interface width W as (Huang et al., 2009),

$$
a = \frac{3\sigma}{4W}, \tag{5}
$$

$$
\kappa = \frac{3\sigma W}{8}. \tag{6}
$$

The chemical potential μ is calculated by taking the variation of the free energy functional with respect to ϕ, and upon substitution of equation (2), it reads,

$$
\mu = \frac{\delta\mathcal{F}}{\delta\phi} = \frac{d\Psi(\phi)}{d\phi} - \kappa\nabla^2\phi = 4a\phi(\phi^2 - 1) - \kappa\nabla^2\phi, \tag{7}
$$

where $\nabla^2 = \boldsymbol{\nabla}\cdot\boldsymbol{\nabla}$ is the (general) Laplacian operator. The evolution of ϕ is governed by the convective Cahn-Hilliard equation (CHE) (Jacqmin, 1999; Badalassi et al., 2003; Briant and Yeomans, 2004), which, with the assumption of a constant mobility M, reads,

$$
\frac{\partial\phi}{\partial t} + (\boldsymbol{u}\cdot\boldsymbol{\nabla})\phi = M\nabla^2\mu. \tag{8}
$$

It is worth noting that the Laplacian operator in cylindrical coordinate (r, θ, z) differs from the common one in Cartesian coordinate (x, y, z); for axisymmetric problems $(\frac{\partial}{\partial\theta} = 0)$, it reads,

$$
\nabla^2_{\text{axisym}} = \left(\frac{\partial^2}{\partial r^2} + \frac{1}{r}\frac{\partial}{\partial r} + \frac{\partial^2}{\partial z^2} \right). \tag{9}
$$

In the absence of azimuthal flows, $u_\theta = 0$, the convective term in equation (8) may be expanded as,

$$
(\boldsymbol{u}\cdot\boldsymbol{\nabla})\phi = u_r\frac{\partial\phi}{\partial r} + u_z\frac{\partial\phi}{\partial z}, \tag{10}
$$

where u_r and u_z are the velocity components in the $r-$ and $z-$ directions, respectively.

2.2 VS formulation for hydrodynamics

As mentioned before, incompressible flows are governed by the incompressible NSEs. For simplicity, we consider the relatively simple situation in which both fluids have *the same density and viscosity*. The governing equations in the VS formulation in cylindrical coordinate (r, θ, z) for axisymmetric problems (i.e., $\frac{\partial}{\partial\theta} = 0$) with no azimuthal flows (i.e., $u_\theta = 0$) read,

$$
u_r = \frac{1}{r}\frac{\partial\tilde{\psi}}{\partial z}, \quad u_z = -\frac{1}{r}\frac{\partial\tilde{\psi}}{\partial r}, \tag{11}
$$

$$
\frac{\partial^2\tilde{\psi}}{\partial z^2} + \frac{\partial^2\tilde{\psi}}{\partial r^2} = r\omega - u_z, \tag{12}
$$

$$
\begin{aligned}
&\frac{\partial\omega}{\partial t} + u_r\frac{\partial\omega}{\partial r} + u_z\frac{\partial\omega}{\partial z} - \frac{u_r\omega}{r} \\
&= \nu\left(\nabla^2_{\text{axisym}}\omega - \frac{\omega}{r^2} \right) + \left(\frac{\partial\tilde{\mu}}{\partial z}\frac{\partial\phi}{\partial r} - \frac{\partial\tilde{\mu}}{\partial r}\frac{\partial\phi}{\partial z} \right),
\end{aligned} \tag{13}
$$

where the first line, equation (11), is from the definition of the streamfunction $\tilde{\psi}$ (Chen et al., 2008a), the third, equation (13), describes the evolution of the vorticity ω (Peyret, 2002) (in general, the vorticity is a vector, and strictly speaking, ω is only the $\theta-$component of the vorticity vector) with the last two terms representing the contribution to the change of vorticity from the interfacial tension force, and the second, equation (12), represents the relation between the streamfunction and the vorticity (Chen et al., 2008a). Note that ν is the kinematic viscosity and $\tilde{\mu} = \frac{\mu}{\rho_c}$ is the chemical potential scaled by the characteristic density ρ_c. For convenience, we used the Laplacian operator for axisymmetric problems defined in equation (9); besides, in what follows two sets of substitutions, $(x \rightarrow z, \ y \rightarrow r)$ and $(u \rightarrow u_z, \ v \rightarrow u_r)$, are made in order to use the symbols in Cartesian coordinate.

2.3 Boundary conditions

In this work, only two types of boundaries are encountered: stationary wall and symmetric line. For each type of boundary, the BCs for the interface equations are described first, followed by those for the flow equations.

2.3.1 BCs on a stationary wall

Denote the wall as $\partial\Omega$ and its normal vector (pointing into the fluid) as $\boldsymbol{n}$. For the interface equations, when the surface energy in equation (3) is used, the BCs for ϕ and μ read,

$$\kappa\boldsymbol{n}\cdot\boldsymbol{\nabla}\phi|_S = \kappa\frac{\partial\phi}{\partial n}\Big|_S = \frac{d\varphi(\phi)}{d\phi} \tag{14}$$

$$= -\frac{3\sigma}{4}\cos\theta_w(1-\phi_S^2).$$

$$\boldsymbol{n}\cdot\boldsymbol{\nabla}\mu|_{\partial\Omega} = \frac{\partial\mu}{\partial n}\Big|_{\partial\Omega} = 0. \tag{15}$$

On the wall one has $v|_{\partial\Omega} = u|_{\partial\Omega} = 0$, thus the BCs for the streamfunction $\tilde{\psi}$ read,

$$\frac{\partial\tilde{\psi}}{\partial x}\Big|_{\partial\Omega} = 0, \quad \frac{\partial\tilde{\psi}}{\partial y}\Big|_{\partial\Omega} = 0. \tag{16}$$

It is noted that the above two conditions in equation (16) are for the first derivatives of $\tilde{\psi}$. In practice, a reference value of $\tilde{\psi}$ at a selected reference point (say, point A) on the boundary is usually specified (e.g., $\tilde{\psi}_A = 0$). Then, the two conditions in equation (16) may be converted into two conditions with one for the gradient and the other for the function itself through an integration along the boundary. Here, because of the definition of $\tilde{\psi}$ ($\tilde{\psi} = y\psi$), it is required that $\tilde{\psi} = 0$ at $y = 0$ (i.e., $r = 0$, at the axis); thus, when the wall intersects the axis, $\tilde{\psi} = 0$ at the intersection point. The BC for the vorticity ω is obtained simply by applying equation (12) on the wall and using equation (16) simultaneously. For instance, on the upper wall where $y = L_y$ (assuming the domain height to be L_y), $u = 0$ ($\frac{\partial\tilde{\psi}}{\partial y} = 0$), and $v = 0$ ($\frac{\partial\tilde{\psi}}{\partial x} = 0$), therefore from equation (12) one has,

$$\omega|_{y=L_y} = \frac{1}{L_y}\frac{\partial^2\tilde{\psi}}{\partial y^2}\Big|_{y=L_y}, \tag{17}$$

which may be further approximated through suitable discretisations using the condition $\frac{\partial\tilde{\psi}}{\partial y}|_{y=L_y} = 0$ (the details will be given later in Section 2.5.4).

2.3.2 BCs on a symmetric line

On the axis $y = 0$ (a line of symmetry), for the PF variables, one has,

$$\frac{\partial\phi}{\partial y}\Big|_{y=0} = 0, \quad \frac{\partial\mu}{\partial y}\Big|_{y=0} = 0, \tag{18}$$

and for the velocity,

$$\frac{\partial u}{\partial y}\Big|_{y=0} = 0, \quad v|_{y=0} = 0 \left(\text{and } \frac{\partial v}{\partial x}\Big|_{y=0} = 0\right). \tag{19}$$

From the above one obtains,

$$\omega|_{y=0} = 0. \tag{20}$$

This avoids the singularity problem in equation (13) where the factor $\frac{1}{y}$ appears. For the streamfunction $\tilde{\psi}$, one has,

$$\tilde{\psi}|_{y=0} = 0. \tag{21}$$

For a symmetric line along the other direction (say, $x = 0$), the BCs are similar:

$$\frac{\partial\phi}{\partial x}\Big|_{x=0} = 0, \quad \frac{\partial\mu}{\partial x}\Big|_{x=0} = 0, \tag{22}$$

$$\omega|_{x=0} = 0, \tag{23}$$

$$\tilde{\psi}|_{x=0} = 0, \tag{24}$$

where the last equation for $\tilde{\psi}$ is obtained through integration along the line with the condition $u|_{x=0} = -\frac{1}{y}\frac{\partial\tilde{\psi}}{\partial y}|_{x=0} = 0$.

2.4 Dimensionless parameters and equations

Suppose we have a characteristic density ρ_c, a characteristic length L_c, and a characteristic velocity U_c, from which a characteristic time is derived as $T_c = \frac{L_c}{U_c}$. With these characteristic quantities, the dimensionless governing equations read (note: for brevity the same symbols are used for the dimensionless variables),

$$v = \frac{1}{y}\frac{\partial\tilde{\psi}}{\partial x}, \quad u = -\frac{1}{y}\frac{\partial\tilde{\psi}}{\partial y}, \tag{25}$$

$$\frac{\partial^2\tilde{\psi}}{\partial x^2} + \frac{\partial^2\tilde{\psi}}{\partial y^2} = y\omega - u, \tag{26}$$

$$\begin{aligned}&\frac{\partial\omega}{\partial t} + u\frac{\partial\omega}{\partial x} + v\frac{\partial\omega}{\partial y}\\ &= \frac{1}{Re}\nabla^2_{\text{axisym}}\omega + \frac{1}{We}\left(\frac{\partial\mu}{\partial x}\frac{\partial\phi}{\partial y} - \frac{\partial\mu}{\partial y}\frac{\partial\phi}{\partial x}\right)\\ &+ \frac{\omega}{y}\left(v - \frac{1}{Re}\frac{1}{y}\right),\end{aligned} \tag{27}$$

$$\frac{\partial\phi}{\partial t} + u\frac{\partial\phi}{\partial x} + v\frac{\partial\phi}{\partial y} = \frac{1}{Pe}\nabla^2_{\text{axisym}}\mu, \tag{28}$$

$$\mu = \frac{1}{Cn}[3\phi(\phi^2-1)] - Cn\left(\frac{3}{8}\nabla^2_{\text{axisym}}\phi\right), \tag{29}$$

where $We = \frac{\rho_c U_c^2 L_c}{\sigma}$ is the Weber number, $Re = \frac{U_c L_c}{\nu}$ is the Reynolds number, $Cn = \frac{W}{L_c}$ is the Cahn number, and $Pe = \frac{U_c L_c^2}{M\sigma}$ is the Peclet number. In addition, the capillary number is defined as $Ca = \frac{\rho_c \nu U_c}{\sigma}$, and We can be expressed as $We = ReCa$. As is well known, the Reynolds number reflects the ratio of inertia force to viscous force. For multiphase flows, the capillary number reflects the ratio of the viscous force over the interfacial tension force. Thus, We measures the ratio of inertia force to the interfacial tension force. By definition, Cn measures the interface width in terms of the characteristic length, and Pe reflects the ratio of convection over diffusion in the CHE. Note that both Cn and Pe are computational parameters of the PF model.

2.5 Finite-difference method for spatial discretisation

2.5.1 Mesh and the discrete variables

In this work we consider cases with the spatial domain being a rectangle specified by $0 \leq x \leq L_x$, $0 \leq y \leq L_y$. The mesh is composed of uniform squares with the side length $\delta_x = \delta_y = h$. The vorticity ω and streamfunction $\tilde{\psi}$ are defined at cell vertex whereas the PF variables (including ϕ and μ) are defined at cell centre (see Figure 1). Suppose L_x and L_y are divided into N_x and N_y uniform segments respectively, i.e., $L_x = N_x h$, $L_y = N_y h$, then one has the following discrete variables, $\omega_{i,j}$ and $\tilde{\psi}_{i,j}$, at the cell vertices,

$$(x_{i,j}, y_{i,j}) = (ih, jh), \text{ for } 0 \leq i \leq N_x, \ 0 \leq j \leq N_y,$$

and the discrete variables, $\phi_{i-\frac{1}{2},j-\frac{1}{2}}$ and $\mu_{i-\frac{1}{2},j-\frac{1}{2}}$, at the cell centres,

$$(x_{i-\frac{1}{2},j-\frac{1}{2}}, y_{i-\frac{1}{2},j-\frac{1}{2}}) = \left(\left(i - \frac{1}{2}\right)h, \left(j - \frac{1}{2}\right)h \right),$$
$$\text{for } 0 \leq i \leq N_x + 1, \ 0 \leq j \leq N_y + 1.$$

Note that for the variables at cell centre, a ghost layer is added outside of the domain so that the BCs are implemented more easily. Besides, the velocity components u and v in the vorticity evolution equation, equation (27), and those in the CHE, equation (28), are treated differently (details will be given later).

**Figure 1** Mesh and the definition of discrete variables
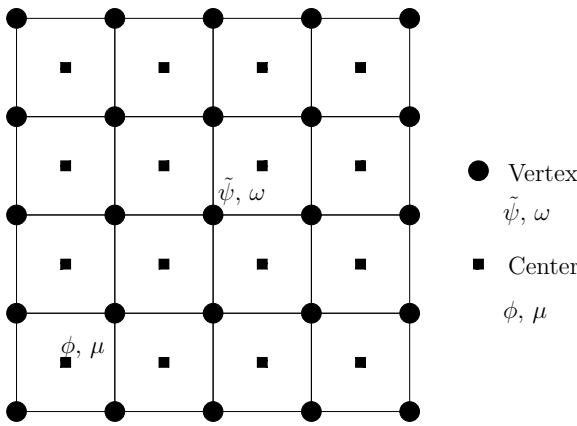
2.5.2 Finite-difference discretisation of spatial derivatives

There are many finite-difference schemes for the approximation of spatial derivatives, which may have different orders of accuracy and different stability properties. In this work, we mainly consider the following two schemes:

1   the common 2nd-order centred scheme (denoted as 2nd)

2   another scheme based on the D2Q9 velocity model (illustrated in Figure 2) in the lattice Boltzmann method (LBM) (Chen and Doolen, 1998) (denoted as iso for the reason to be given below).

Figure 2 D2Q9 velocity model in the lattice Boltzmann method
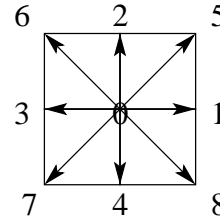
In order to describe the schemes it is necessary to introduce the D2Q9 velocity model first. Without losing the core feature, the (scaled) D2Q9 velocity model (assuming the lattice velocity is unit) may be expressed as,

$$\boldsymbol{e}_k = \begin{cases} (0,0) & \text{for } k = 0 \\ (\cos[\frac{(k-1)\pi}{2}], & \text{for } k = 1,2,3,4 \\ \sin[\frac{(k-1)\pi}{2}]) & \\ (\cos[\frac{(2k-9)\pi}{4}], & \text{for } k = 5,6,7,8 \\ \sin[\frac{(2k-9)\pi}{4}]) \end{cases}, \tag{30}$$

where k is the index to number the velocity vector set. This set of velocity vectors connects a point (say, at $\boldsymbol{x}_{i,j} = (x_i, y_j)$) with its four nearest neighbours (at $\boldsymbol{x}_{i,j} + \boldsymbol{e}_k \delta_x$, $k = 1,2,3,4$) and also with its four next-to-nearest neighbours (at $\boldsymbol{x}_{i,j} + \boldsymbol{e}_k \delta_x$, $k = 5,6,7,8$). The scheme 2nd is rather standard, and for brevity it is not described here. When the scheme iso is used, the first derivatives and the (usual) Laplacian (in Cartesian coordinates) of a twice differentiable function f are calculated as,

$$\left.\frac{\partial f}{\partial x}\right|_{i,j} = \frac{3}{\delta_x} \sum_{k=1}^{8} w_k e_{kx} f(\boldsymbol{x}_{i,j} + \boldsymbol{e}_k \delta_x), \tag{31}$$

$$\left.\frac{\partial f}{\partial y}\right|_{i,j} = \frac{3}{\delta_x} \sum_{k=1}^{8} w_k e_{ky} f(\boldsymbol{x}_{i,j} + \boldsymbol{e}_k \delta_x), \tag{32}$$

$$\left.\left(\frac{\partial^2 f}{\partial x^2} + \frac{\partial^2 f}{\partial y^2}\right)\right|_{i,j} \tag{33}$$
$$= \frac{6}{\delta_x^2}\left[\sum_{k=1}^{8} w_k f(\boldsymbol{x}_{i,j} + \boldsymbol{e}_k \delta_x) - (1 - w_0)f(\boldsymbol{x}_{i,j})\right],$$

where w_k is the weight for different velocities,

$$w_k = \begin{cases} \frac{4}{9} & \text{for } k = 0 \\ \frac{1}{9} & \text{for } k = 1,2,3,4 \\ \frac{1}{36} & \text{for } k = 5,6,7,8 \end{cases}, \tag{34}$$

and e_{kx} and e_{ky} denote the $x-$ and $y-$components of the vector $\boldsymbol{e}_k$. This scheme is also 2nd-order accurate and has better isotropic property (thus denoted as iso). It should be noted that in this work the scheme iso is only used in the equations for interface dynamics, including equations (28) and (29). In some previous studies, the scheme iso was found to reduce the spurious velocity in the interfacial region of multiphase flows (Tiribocchi et al., 2009). Our experience indicates that it is also more stable than the scheme 2nd. We shall make some comparisons between the two schemes for certain cases under the current implementation in Section 3. For most of the problems studied in this work, the *default* scheme for the spatial derivatives in the interface equations, Equations (28) and (29), is the scheme iso.

2.5.3   Data exchange on stagger grid

As noted in Section 2.5.1, ω and $\tilde{\psi}$ are defined at cell vertex whereas ϕ and μ are defined at cell centre. Each of the two sets of governing equations contains some variables or terms that need the information from the other. The CHE, equation (28), need the velocity components u and v at cell centre, which are obtained from $\tilde{\psi}$ at the four surrounding vertices (see Figure 3),

$$u_{i-\frac{1}{2},j-\frac{1}{2}} = -\frac{1}{2}\frac{1}{y_{i-\frac{1}{2},j-\frac{1}{2}}}\left(\left.\frac{\partial\tilde{\psi}}{\partial y}\right|_L + \left.\frac{\partial\tilde{\psi}}{\partial y}\right|_R\right), \quad (35)$$

$$v_{i-\frac{1}{2},j-\frac{1}{2}} = \frac{1}{2}\frac{1}{y_{i-\frac{1}{2},j-\frac{1}{2}}}\left(\left.\frac{\partial\tilde{\psi}}{\partial x}\right|_{Low} + \left.\frac{\partial\tilde{\psi}}{\partial x}\right|_{Up}\right), \quad (36)$$

where the partial derivatives on the four sides are approximated by,

$$\left.\frac{\partial\tilde{\psi}}{\partial y}\right|_L = \frac{1}{h}(\tilde{\psi}_{i-1,j} - \tilde{\psi}_{i-1,j-1}), \quad (37)$$

$$\left.\frac{\partial\tilde{\psi}}{\partial y}\right|_R = \frac{1}{h}(\tilde{\psi}_{i,j} - \tilde{\psi}_{i,j-1}),$$

$$\left.\frac{\partial\tilde{\psi}}{\partial x}\right|_{Low} = \frac{1}{h}(\tilde{\psi}_{i,j-1} - \tilde{\psi}_{i-1,j-1}),$$

$$\left.\frac{\partial\tilde{\psi}}{\partial x}\right|_{Up} = \frac{1}{h}(\tilde{\psi}_{i,j} - \tilde{\psi}_{i-1,j}). \quad (38)$$

On the other hand, the vorticity evolution equation, equation (27), contains two terms that account for the contribution from the interfacial tension force involving $\frac{\partial\phi}{\partial x}$, $\frac{\partial\phi}{\partial y}$, $\frac{\partial\mu}{\partial x}$ and $\frac{\partial\mu}{\partial y}$. They are evaluated using the PF variables at the surrounding cell centres in a similar way.

It should be noted that $u_{i,j}$ and $v_{i,j}$ in the discretised vorticity evolution equation are obtained directly at the vertices from the streamfunction $\tilde{\psi}$ using equation (25) and the scheme 2nd. Although one has the option to obtain $u_{i,j}$ and $v_{i,j}$ from those already found at the surrounding cell centres by arithmetic averaging, numerical tests show that it could cause some problems near the axis under certain conditions. By contrast, the first way performs much better.

Figure 3   Calculation of the velocity components u and v at cell centre from the streamfunction at cell vertex
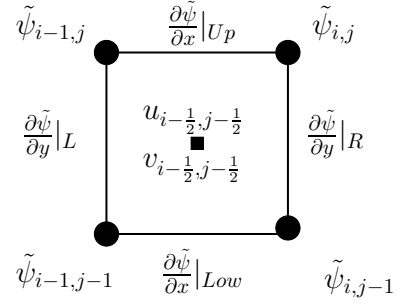
2.5.4   BCs in discrete form

With the above spatial discretisations, some of the BCs about derivatives given in Section 2.3 may be converted into their respective discrete forms. For example, the discrete form for equation (17) reads,

$$\omega_{i,j}|_{j=N_y} = \frac{2}{L_y}\frac{\tilde{\psi}_{i,N_y-1} - \tilde{\psi}_{i,N_y}}{h^2}, \quad (39)$$

where the condition $\left.\frac{\partial\tilde{\psi}}{\partial y}\right|_{y=L_y} = 0$ has been used. Equation (39) may be regarded as a variant of Thom's formula (see E and Liu, 1996 and references therein). On other walls, the discrete BC for the vorticity ω may be written in a similar manner. For all cases considered in this work, the streamfunction $\tilde{\psi}$ vanishes on all boundaries.

As noted in Section 2.5.1, for the PF variables defined at cell centre, the BCs are implemented through a ghost layer added outside of the domain. Take ϕ and μ at the axis ($y = 0$) as an example. Upon discretisation, equation (18) becomes,

$$\left.\frac{\partial\phi}{\partial y}\right|_{y=0} \approx \frac{\phi_{i-\frac{1}{2},\frac{1}{2}} - \phi_{i-\frac{1}{2},-\frac{1}{2}}}{h} = 0,$$

$$\left.\frac{\partial\mu}{\partial y}\right|_{y=0} \approx \frac{\mu_{i-\frac{1}{2},\frac{1}{2}} - \mu_{i-\frac{1}{2},-\frac{1}{2}}}{h} = 0, \quad (40)$$

from which ϕ and μ at the ghost layer $y = -\frac{h}{2}$ are obtained as,

$$\phi_{i-\frac{1}{2},-\frac{1}{2}} = \phi_{i-\frac{1}{2},\frac{1}{2}}, \quad \mu_{i-\frac{1}{2},-\frac{1}{2}} = \mu_{i-\frac{1}{2},\frac{1}{2}}. \quad (41)$$

In equation (14) it is required to have ϕ_S before knowing the normal gradient on a wall. Here we use a simple approximation to find ϕ_S. Suppose the wall is at $y = 0$, we just set $\phi_S \approx \phi_{i-\frac{1}{2},\frac{1}{2}}$.

2.6   Temporal discretisation

With the spatial derivatives approximated by the finite-difference schemes, the two main evolution equations, equation (27) and equation (28), become two ordinary differential equations, which have to be discretised in time. Here the common explicit 4th-order Runge-Kutta (RK4) method is adopted.

In the present work, all variables are updated at the same discrete times (i.e., $t = 0$, δ_t, $2\delta_t$, $\cdots$). That reduces the complexity of the coupling between the hydrodynamics and interface dynamics to some degree. The time marching of the equation system involving equations (25), (26), (27), (28) and (29) is in essence to obtain the main variables at t^{n+1} from those at t^n, i.e.,

$$(\tilde{\psi}^n, \omega^n, \phi^n, \mu^n) \rightarrow (\tilde{\psi}^{n+1}, \omega^{n+1}, \phi^{n+1}, \mu^{n+1}). \tag{42}$$

One can do the marching for the CHE first to obtain (ϕ^{n+1}, μ^{n+1}), and then carry out the steps for the flow equations in VS formulation with (ϕ^{n+1}, μ^{n+1}) being used to evaluate the contributions due to interfacial tension forces. Instead, one can also do the marching for the flow equations first, followed by that for the CHE. Some numerical tests show that the change of the order affects the results only very slightly. Here the first option is used, and the detailed steps to be carried out from $t^n (= 0)$ to $t^{n+1} (= \delta_t)$ are as follows,

1   to initialise the main variables at cell vertex (everywhere, i.e., in the bulk region and at all boundaries), including $(\tilde{\psi}^n_{i,j}, \omega^n_{i,j})$ and also those at cell centre (bulk region only), including $(\phi^n_{i-\frac{1}{2},j-\frac{1}{2}}, \mu^n_{i-\frac{1}{2},j-\frac{1}{2}})$, and also calculate the PF variables in the ghost layers

2   to calculate the velocity $(u^n_{i-\frac{1}{2},j-\frac{1}{2}}, v^n_{i-\frac{1}{2},j-\frac{1}{2}})$ at cell centre (bulk region only), using equation (25)

3   to advance the PF variables from t^n to t^{n+1} using equations (28), (29) and appropriate BCs with RK4 time stepping (while freezing the velocity) to obtain $(\phi^{n+1}_{i-\frac{1}{2},j-\frac{1}{2}}, \mu^{n+1}_{i-\frac{1}{2},j-\frac{1}{2}})$ in the bulk region, and update the PF variables in the ghost layers

4   to calculate the contribution of the interfacial tension force to the vorticity at cell vertex in the bulk region using the newly obtained $(\phi^{n+1}_{i-\frac{1}{2},j-\frac{1}{2}}, \mu^{n+1}_{i-\frac{1}{2},j-\frac{1}{2}})$

5   To advance the vorticity from t^n to t^{n+1} using equation (27) with RK4 time stepping (while freezing the streamfunction $\tilde{\psi}$) to obtain $\omega^{n+1}_{i,j}$ in the bulk region

6   to solve the Poisson-like equation, equation (26), with given BCs to obtain $\tilde{\psi}^{n+1}_{i,j}$ in the bulk region

7   to update the vorticity $\omega^{n+1}_{i,j}$ on the wall boundaries using the newly obtained $\tilde{\psi}^{n+1}_{i,j}$

8   to go back to step (2) and prepare for the next time marching cycle.

It is noted that in Step (6) some iterations may be required. Besides, in Step (1) only $\phi^n_{i-\frac{1}{2},j-\frac{1}{2}}$ is actually given at the beginning and $\mu^n_{i-\frac{1}{2},j-\frac{1}{2}}$ is calculated from equation (29) with suitable BCs which give $\phi^n_{i-\frac{1}{2},j-\frac{1}{2}}$ in the ghost layers. That takes a few sub-steps, and such sub-steps are performed in Step (3) as well.

To start a simulation, appropriate initial conditions must be provided. For $\tilde{\psi}$ and ω, the initial conditions must be compatible with equation (26) (in our simulation, we have paid attention to satisfy this requirement). In addition, the initial fields depend on the specific problem being studied (to be described in detail below).

Here we would like to give some remarks about the time marching schemes. According to E and Liu (1996), the use of RK4 for the vorticity evolution can alleviate the cell Reynolds number constraint. Besides, RK4 has better stability than some other lower-order explicit time marching schemes (like the 1st-order forward Euler and the 2nd-order Runge-Kutta (RK2) method), which makes it relatively popular. Nevertheless, we have also tried RK2 for the vorticity evolution in some problems studied here and no obvious difference was observed while the computation time was reduced significantly. Thus, it might not be necessary to use RK4 for all evolution equations. As the same time, for the Cahn-Hilliard equation, the use of RK2 for certain cases cannot guarantee a stable computation whereas RK4 is fine. For large scale simulations, it is suggested that different time marching schemes may be tried first and the most economic one is used provided that the stability is not compromised.

2.7   Some comparison with the VP formulation

It may be helpful to make some comparison between the VS formulation and the VP formulation. When the VP formulation is used, the hydrodynamic governing equations read,

$$\frac{\partial u_r}{\partial r} + \frac{u_r}{r} + \frac{\partial u_z}{\partial z} = 0, \tag{43}$$

$$\frac{\partial u_r}{\partial t} + \left(u_r \frac{\partial u_r}{\partial r} + u_z \frac{\partial u_r}{\partial z} \right) \tag{44}$$
$$= -\frac{\partial S_p}{\partial r} + \nu \left(\nabla^2_{\text{axisym}} u_r - \frac{u_r}{r^2} \right) - \phi \frac{\partial \tilde{\mu}}{\partial r},$$

$$\frac{\partial u_z}{\partial t} + \left(u_r \frac{\partial u_z}{\partial r} + u_z \frac{\partial u_z}{\partial z} \right) \tag{45}$$
$$= -\frac{\partial S_p}{\partial z} + \nu \nabla^2_{\text{axisym}} u_z - \phi \frac{\partial \tilde{\mu}}{\partial z}.$$

As pointed out by Ferziger and Peric (1999), the most attractive feature of the VS formulation for (pseudo-) 2-D problems is the reduction of dependent variables and equations (which is seen easily through the comparison between equations (11), (12), and (13) and the above three). Besides, one does not have to worry about the continuity equation (i.e., to enforce a divergence-free velocity field) by using the VS formulation. In contrast, the numerical solution of the VP equations are less straightforward. One of the famous methods to solve the VP equations is the projection method by Chorin (1968), which may be taken for comparison here. In the projection method, the time marching from $\boldsymbol{u}^n$ (the velocity vector at t^n: $\boldsymbol{u}^n = [u^n_r, u^n_z]^T$) to $\boldsymbol{u}^{n+1}$ is divided into two steps

by introducing an intermediate vector $\boldsymbol{u}^*$: in the first sub-step from $\boldsymbol{u}^n$ to $\boldsymbol{u}^*$, the pressure term $\boldsymbol{\nabla}S_p$ is excluded; in the second sub-step from $\boldsymbol{u}^*$ to $\boldsymbol{u}^{n+1}$, the viscous terms are excluded whereas the pressure term $\boldsymbol{\nabla}S_p$ is treated (which requires to solve a Poisson(-like) equation). As compared with the VS formulation, an additional evolution equation with terms nearly as complex as the evolution equation for the vorticity [c.f. equation (13)] has to be handled, which reduces the efficiency of the method to some extent. Of course, the relative increase of computational cost depends on many factors like the schemes for derivative evaluation and for time stepping. A rough estimate suggests that, when an explicit time stepping scheme is used, the increase may not be quite significant because the most time-consuming part is the solution of the Poisson(-like) equation, which cannot be avoided in either the VS or VP formulation. However, when an implicit (or a semi-implicit) time stepping scheme is used, the marching of the evolution equation would require a solver almost as expensive as the Poisson solver. In that case the increase of computational cost by using the VP formulation will be much more appreciable. As more detailed quantitive comparisons regarding the computational efficiency require the development of another fully-functional solver using the VP formulation for incompressible axisymmetric two-phase flows, we would not carry it out in the present work.

3 Results and discussions

3.1 Characteristic quantities and dimensionless numbers

In Section 2.4, the dimensionless equations were derived and the important dimensionless parameters were identified. Here we revisit the characteristic quantities and dimensionless parameters, but now with the specific problems to be studied (a single drop or two drops of equal size) in mind. In each problem, there is a drop of radius R, which is chosen to be the characteristic length L_c. The constant density is selected as the characteristic density ρ_c. Following Khatavkar et al. (2007), we use a characteristic velocity U_c defined solely based on the fluid properties as,

$$U_c = \frac{\sigma}{\rho_c \nu}. \tag{46}$$

Note that from the physical properties and the drop radius R another velocity scale U_σ may also be derived (Thoroddsen et al., 2005),

$$U_\sigma = \sqrt{\frac{\sigma}{\rho_c R}}. \tag{47}$$

Here we mainly use on U_c (though U_σ may also be used for certain cases). From L_c and U_c, the characteristic time T_c is found to be,

$$T_c = \frac{L_c}{U_c} = \frac{R\rho_c \nu}{\sigma}. \tag{48}$$

All quantities of length, time and velocity below are scaled by L_c, T_c and U_c, respectively (unless otherwise specified). With the above definitions of characteristic quantities, the capillary number is found to be $Ca = \frac{\rho_c \nu U_c}{\sigma} = 1$ and the Reynolds number is,

$$Re = \frac{U_c R}{\nu} = \frac{\sigma}{\rho_c \nu} \frac{R}{\nu} = \frac{\sigma R}{\rho_c \nu^2}. \tag{49}$$

In addition, the Weber number (as defined in Section 2.4) is found to be $We = ReCa = Re$ (as $Ca = 1$). It should be noted that Ca and Re defined in this way do not reflect the *actual* physics of the problem because the velocity scale U_c is only based on the fluid properties (rather than the flow characteristics), but they are useful in setting up the simulation. If the other velocity scale U_σ is used, another Reynolds number may be obtained as (Thoroddsen et al., 2005),

$$Re_\sigma = \frac{U_\sigma R}{\nu} = \sqrt{\frac{\sigma R}{\rho_c \nu^2}} = \sqrt{Re}. \tag{50}$$

This Reynolds number Re_σ is useful for some problems (e.g., drop coalescence to be studied below). In addition, the Ohnesorge number Oh is also often used for drop dynamics (Ding et al., 2012):

$$Oh = \frac{\rho_c \nu}{\sqrt{\rho_c \sigma R}}, \tag{51}$$

and it is related to the other dimensionless numbers as $Oh = 1/\sqrt{Re} = 1/Re_\sigma$. In Section 2.4, two other parameters related to the PF model were also defined: the Cahn number Cn and the Peclet number Pe. Using the characteristic quantities $L_c(= R)$ and U_c given by equation (46), it is easy to find the individual values of Cn and Pe for each problem below. We note that different people may use slightly different definition of the interface width. For instance, the interface width ε in Yue et al. (2010) and Ding et al. (2007) is related to the present one as $\varepsilon = W/(2\sqrt{2})$. Thus, the Cahn number based on ε, Cn_ε, is related to the present Cn as, $Cn_\varepsilon = Cn/(2\sqrt{2}) \approx 0.35Cn$. In addition, Yue et al. (2010) proposed the use of another parameter S for problems involving contact lines, which reflects the ratio of the diffusion length scale at the contact line $l_D = \sqrt{M(\rho_c \nu)}$ over the characteristic length L_c, and is thus given by $S = \sqrt{M(\rho_c \nu)}/L_c$.

3.2 Common problem setup and quantities of interest

As noted in Section 2.5.1, the domain is a rectangle of size $L_x \times L_y$ and the origin is located at the lower-left corner. In all simulations, the lower side of the domain is the symmetric axis ($y = 0$) on which the symmetric BCs are applied; on the upper and right sides solid walls are assumed. The left side is either a wall or a symmetric line depending on the specific problem (if it is a symmetric line, then only the upper-right quarter is actually considered). To use a relatively large domain reduces the effects of the surrounding walls, but increases the computational cost. Here, L_x and L_y are chosen to balance the two sides. Note

that the force due to gravity is omitted. This is reasonable when the scale of the problem is very small or when the drop is in a microgravity environment.

The simulations are performed in the range $0 \leq t \leq t_e$, where t_e (measured in T_c) denotes the time at the end of the simulation. Suppose the characteristic length L_c (the drop radius R) is discretised by N_L uniform segments and the characteristic time T_c is discretised by N_t uniform segments, then one has,

$$\delta_x = \frac{L_c}{N_L}\left(= \frac{L_x}{N_x} = \frac{L_y}{N_y} = h\right), \quad \delta_t = \frac{T_c}{N_t}. \quad (52)$$

In all problems, initially there is no flow. Thus, the initial streamfunction $\tilde{\psi}$ and vorticity ω are,

$$\tilde{\psi}^0_{i,j} = 0, \quad \omega^0_{i,j} = 0. \quad (53)$$

The initial position of the drop centre is $(x_c, y_c) = (x_c, 0)$ (i.e., always on the axis). The initial order parameter ϕ field is given by,

$$\phi^0_{i-\frac{1}{2},j-\frac{1}{2}} = -\tanh\left(\frac{2(r_{i-\frac{1}{2},j-\frac{1}{2}} - R)}{W}\right), \quad (54)$$

where $r_{i-\frac{1}{2},j-\frac{1}{2}} = \sqrt{(x_{i-\frac{1}{2}} - x_c)^2 + (y_{j-\frac{1}{2}} - y_c)^2}$ is the distance between the cell centre $(x_{i-\frac{1}{2}}, y_{j-\frac{1}{2}})$ and the drop centre (x_c, y_c). The initial velocities at cell centre, $u^0_{i-\frac{1}{2},j-\frac{1}{2}}$ and $v^0_{i-\frac{1}{2},j-\frac{1}{2}}$, and the initial chemical potential $\mu^0_{i-\frac{1}{2},j-\frac{1}{2}}$ may be computed from $\tilde{\psi}^0_{i,j}$ and $\phi^0_{i-\frac{1}{2},j-\frac{1}{2}}$ using the respective equations and BCs given in Section 2.

For the flow field, we are interested in the maximum velocity magnitude over the whole domain at time t,

$$\sqrt{u^2 + v^2}|_{\max}(t) \quad (55)$$
$$= \max_{1 \leq i \leq N_x, 1 \leq j \leq N_y} \sqrt{(u_{i-\frac{1}{2},j-\frac{1}{2}}(t))^2 + (v_{i-\frac{1}{2},j-\frac{1}{2}}(t))^2}.$$

In addition, for convenience, we define the maximum velocity magnitude during the whole simulation as,

$$U_{\max} = \max_{0 \leq t \leq t_e} \sqrt{u^2 + v^2}|_{\max}(t). \quad (56)$$

As noted above in Section 3.1, the actual Reynolds number usually differs from that given by equation (49). With $U_{\max}$, we can calculate another Reynolds number $Re_{\max}$ as,

$$Re_{\max} = \frac{U_{\max}R}{\nu} = U_{\max}Re, \quad (57)$$

where we have used the condition that the velocities in equation (56) are already scaled by U_c. This Reynolds number $Re_{\max}$ is supposed to reflect the actual physics of the problem better than Re.

3.3 Test of Laplace law for a quiescent drop

The first problem studied is a quiescent drop. For this problem, the common physical parameter is $Ca = 1$. Some studies of this problem have been presented in another paper (Huang et al., 2013), together with some comparisons

between the method proposed here and that in Huang et al. (2013), which is a hybridisation of the LBM using the multiple-relaxation-time (MRT) collision model and the finite-difference method (following the notations in Huang et al., 2013, the present method is denoted as NSCH-VS(FD) and that method is denoted as MRT-LB-FD). The two methods differ from each other substantially in the way to deal with the hydrodynamics and also in the way to couple the flow and interface dynamics. Therefore, good agreements between them serve the purpose to verify each other. For conciseness, the results already presented in Huang et al. (2013) are not replicated here. But for clarity and completeness some essential descriptions of the problem are still given. Unlike Huang et al. (2013), here to reduce the computational cost, the left side is a symmetric line. Thus, only (the right) half of the domain in Huang et al. (2013) is used. The domain size is $L_x \times L_y = 2 \times 2$, and the drop centre is $(x_c, y_c) = (0, 0)$.

The initial order parameter ϕ field given in equation (54) does not correspond to the equilibrium state for an interface with finite curvature. The CHE provides a diffusional mechanism to drive the order parameter field to evolve towards the *true* equilibrium state (Yue et al., 2007). Upon reaching equilibrium, the order parameters inside and outside the drop become $\phi^{eq}_{in} = 1 + \epsilon^{eq}_{in}$ and $\phi^{eq}_{out} = -(1 - \epsilon^{eq}_{out})$ (ϵ^{eq}_{in} and ϵ^{eq}_{out} take some small positive values), which satisfy the Laplace law,

$$(\Delta p)^{eq} = (p^{ma}_{in} - p^{ma}_{out})^{eq} \approx p^b_{in}(\phi^{eq}_{in}) - p^b_{out}(\phi^{eq}_{out}) \quad (58)$$
$$= \frac{\sigma}{2R^{eq}_d},$$

where R^{eq}_d is the drop radius in equilibrium, p^b is the *bulk pressure* (i.e., pressure of the bulk fluid excluding gradient and dynamic effects (see Papatzacos, 2002), similar to the *thermodynamic pressure* defined by Lee and Lin (2005)) related to ϕ through the *equation of state*,

$$p^b = \phi\frac{d\Psi(\phi)}{d\phi} - \Psi(\phi), \quad (59)$$

and p^{ma} is the modified overall pressure related to p^b as (note a modified pressure $p^m = p^b - (\kappa\phi\nabla^2\phi - \frac{1}{2}\kappa|\nabla\phi|^2)$ was defined by Lee and Lin (2005), which has a much smoother variation across an interface than the bulk pressure p^b),

$$p^{ma} = S_p + p^b - \left(\kappa\phi\nabla^2\phi - \frac{1}{2}\kappa|\nabla\phi|^2\right). \quad (60)$$

where S_p is the *hydrodynamic pressure* and cannot be obtained directly using the VS formulation. However, for the study of a quiescent drop its variation is much smaller than that of p^b. Besides, in equilibrium there is no flow, and S_p is uniform. Thus, it may be neglected when the pressure difference is calculated. What is more, away from the interface, both $\nabla^2\phi$ and $\nabla\phi$ (almost) vanish. Therefore, one has $p^{ma} \approx p^b$ in equilibrium. During the evolutionary process, the drop shrinks a little bit, of which the extent depends on the Cahn number Cn and the speed depends

on the Peclet number Pe (Yue et al., 2007). After the equilibrium state is achieved, the drop radius R_d^{eq} is slightly smaller than the initial one R. As in Huang et al. (2013), the inside and outside order parameters were sampled at the drop centre and some point that is $R_d^{eq} + 2Cn$ away from the drop centre respectively, so that neither is in the interfacial region. The drop radius in equilibrium R_d^{eq} was computed as $(R_x^{eq} + R_y^{eq})/2$ where R_x^{eq} and R_y^{eq} are the equilibrium radii along the $x-$axis and in $y-$direction along the vertical line passing through the centre, respectively (note R_x^{eq} and R_y^{eq} are almost the same when the interface width W is large enough, as in most cases below). During the simulation, we monitor the difference of the bulk pressure $\Delta p^b = p_{in}^b - p_{out}^b$, the drop radius R_d, and compare the quantity Δp^b with the pressure difference expected in equilibrium $\sigma/(2R_d)$ through the relative deviation $\delta(\Delta p)$,

$$\delta(\Delta p) = \frac{\Delta p^b - \sigma/(2R_d)}{\sigma/(2R_d)} \times 100\%. \quad (61)$$

Note that upon reaching equilibrium the difference is expected to (nearly) vanish. Unlike Huang et al. (2013), here we mainly examine the quantity $2R_d^{eq}(\Delta p)^{eq}$ (which is sort of the numerically measured interfacial tension) under different Weber numbers and also the effect of using different Cahn numbers Cn (interface width W) while fixing the characteristic length L_c.

3.3.1 The quantity $2R_d^{eq}(\Delta p)^{eq}$ under various We numbers

The quantity $2R_d^{eq}(\Delta p)^{eq}$ is supposed to be equal to the interfacial tension σ. Figure 4 shows the variations of the quantity $2R_d^{eq}(\Delta p)^{eq}$ and σ with We with both axes plotted in logarithmic scale. Four Weber numbers ($We = 25, \ 100, \ 10^3, 10^4$) were tested to obtain this figure while other parameters were fixed to be $Cn = 0.15$, $Pe = 4 \times 10^3$, $N_L = 20$, $N_t = 80$. The quantity $2R_d^{eq}(\Delta p)^{eq}$ was measured after $t = 10^3$. It is easy to see from the definition of We that the (dimensionless) interfacial tension is inversely proportional to We. In Figure 4 it is observed that the quantity $2R_d^{eq}(\Delta p)^{eq}$ varies with We almost following this way and it agrees with σ very well. Detailed examinations show that the deviations of the quantity $2R_d^{eq}(\Delta p)^{eq}$ from σ are less than 2.5% for all of the Weber numbers.

3.3.2 Effect of Cahn number Cn (interface width W)

Figure 5 shows the evolutions of $\delta(\Delta p)$ at different Cahn numbers $Cn = 0.2, \ 0.1, \ 0.075, \ 0.05$ (or interface widths $W = 6.4, \ 3.2, \ 2.4, \ 1.6 \ (h)$) while other parameters are fixed to be $Re(= We) = 10^3$, $Pe = 2 \times 10^3$, $N_L = 32$, $N_t = 512$. It is noted that initially $\phi_{in} \approx 1.0$ and $\phi_{out} \approx -1.0$, as specified in equation (54), and those lead to $\delta(\Delta p) \approx -100\%$. From Figure 5 it is observed that as time goes on $\delta(\Delta p)$ evolves towards zero when Cn (or W) is large enough (for $Cn = 0.2, \ 0.1, \ 0.075$ or $W = 6.4, \ 3.2, \ 2.4 \ (h)$). By contrast, when $Cn = 0.05$

$(W = 1.6)$, this trend is not observed and $\delta(\Delta p)$ remains between -60% and -70%. This is due to the interface is too thin ($W = 1.6$ only) to allow sufficiently good resolution of the interface profile. Under such a condition, the isotropy of the circular (spherical in 3-D) interface is not preserved; in fact, even when $Cn = 0.075$ ($W = 2.4$) the anisotropy of the interface can already be noticed (not shown here) though the final balance across the interface can still be roughly achieved. On the other hand, when Cn becomes larger (W increases) the interfacial region occupies larger portion of the whole domain and the interfacial dynamics becomes more significant. For instance, Figure 5 shows that it takes longer time for $\delta(\Delta p)$ to become close to zero when $Cn = 0.2$ than in the case with $Cn = 0.1$. For problems with more important macroscopic dynamics this is not desirable. From the convergence point of view, Cn should (in theory) approach zero for usual problems. Therefore, one should use a Cn as small as possible while maintaining a W large enough to resolve the interface (Jacqmin, 1999). Yue et al. (2007) also provided some helpful analyses and comments regarding the convergence to the sharp-interface limit (SIL), which are worth revisiting here. In general the Cahn number Cn should be much less than 1 to approach the SIL, and in the phase-field-based (diffuse-interface) simulations there is an error of $O(Cn^2)$ in the interfacial tension (Yue et al., 2007). It is very attractive to apply adaptive meshing to achieve a small Cn (see, e.g., Yue et al., 2006; Sui and Spelt, 2013b). In the literature, however, many simulations still used uniform meshes (see, e.g., Lee and Liu, 2010; Liu et al., 2013) possibly due to the significant effort required to develop adaptive meshing (it is beyond the scope of this work to incorporate the adaptive meshing strategy into the proposed method). In general, the Cahn number is to be selected to keep the deviation from the SIL reasonably small while maintaining an acceptable computational cost (the smallest Cn acceptable with a uniform mesh can be much larger than that with an adaptive mesh). We have taken the above considerations into account in the studies of other problems below. The typical value of Cn is 0.1 and that of W is 3.2, which indicates that the interface roughly covers three grid points.

3.3.3 Comparison between two schemes: `2nd` vs. `iso`

In Section 2.5.2, two schemes for the spatial derivatives of PF variables in equations (28) and (29) were given. Here, we select one case with $Re(= We) = 10^3$, $Cn = 0.2$, $Pe = 4 \times 10^3$, $N_L = 20$, $N_t = 80$ simply for the purpose to compare the scheme `2nd` with the scheme `iso`. Specifically, we compare the evolutions of the maximum velocity magnitude $\sqrt{u^2 + v^2}|_{\max}$. Figure 6 gives the semi-logarithmic plot of $\sqrt{u^2 + v^2}|_{\max}$'s evolution for the two schemes. The current observations are in general similar to those reported in Huang et al. (2013). It is seen from Figure 6 that $\sqrt{u^2 + v^2}|_{\max}$ remains to be small (less than 5×10^{-4}) during the whole simulation. This is because there are no significant *macroscopic* flows in this problem. From Figure 6, one also finds that $\sqrt{u^2 + v^2}|_{\max}$ shows

some fluctuations initially (especially when the scheme 2nd is used) and keeps decreasing after certain time. For the two schemes, major differences are seen during the segment $0 \leq t \leq 110$; afterwards, they almost overlap. The peak value of $\sqrt{u^2 + v^2}|_{\max}$ (i.e., $U_{\max}$) by 2nd is much larger than that by iso. We have observed that the scheme 2nd is in general less stable than iso, most likely due to the above reason. Although the scheme iso costs (slightly) more computation time, its improved stability makes it more preferable. From equation (57) and Figure 6, one can also estimate that $Re_{\max}$ is about $O(0.1)$ for this particular case (although it is not quite meaningful here because there is not important macroscopic flow).

3.4 Study of drop coalescence

The next problem studied is the coalescence of two drops having the same radius R. Initially both drops are stationary. Their initial centres are given by $(x_{c1}, y_{c1}) = (1, 0)$ and $(x_{c2}, y_{c2}) = (-1, 0)$. That means they are in contact with each other through one point initially (of course, in theory only; actually they have some small region overlapping due to the finite interface width in PF models). The symmetry about the $y-$axis of this problem makes it possible to use only the right half of the domain in simulation. In addition, one has the symmetry about the $x-$axis. The actual domain of simulation adopted here is only a quarter (the upper-right one) of the original domain (the cross section of an enclosed cylinder). On the left the symmetric conditions are applied (see Section 2.3.2 for details). The size of the simulation domain is $L_x \times L_y = 4 \times 4$. Driven by the capillary force in the contact region, the two drops coalesce with each other and the radius of the contact region enclosed by the interface (where $\phi = 0$) at $x = 0$ (denoted as r_b here, somewhat similar to R_y in Section 3.3 above) grows with time. Some previous studies have found a scaling law for the growth of

r_b (Eggers et al., 1999; Duchemin et al., 2003; Wu et al., 2004; Xing et al., 2007),

$$\frac{r_b}{R} = \alpha_g \sqrt{\frac{t}{\tau}}, \tag{62}$$

where $\tau = \sqrt{\rho_c R^3 / \sigma}$ is another characteristic time typically used for inviscid dynamics (Duchemin et al., 2003), and α_g is a constant. Note that α_g may have different values for different flows: for instance, $\alpha_g = 1.62$ for inviscid flows (Duchemin et al., 2003), and it could have lower values (e.g., 1.29, 1.09 and 1.03) for viscous flows (Wu et al., 2004), or even lower ones (e.g., 0.46 and 0.41) under different conditions (Thoroddsen et al., 2005). The characteristic time τ is related to the previous one T_c defined in equation (48) as $\tau = Re_\sigma T_c$, where $Re_\sigma = \sqrt{Re}$ [cf. equation (50)]. As the initial drop radius is chosen to be the characteristic length, when expressed in the scaled variables of the present work, equation (62) becomes,

$$r_b = \alpha_g \sqrt{\frac{t}{Re_\sigma}}. \tag{63}$$

3.4.1 Mass conservation and convergence

Before investigating the physical problem, we carry out some numerical tests on the method to look into its properties. The main focuses include the *mass* conservation and convergence. We monitor a quantity V_d which is proportional to the *mass* of the drop M_d as,

$$\begin{aligned} V_d &= \frac{M_d}{2\pi} \\ &= \int_0^{L_x} \int_0^{L_y} y \frac{1 + \phi(x,y)}{2} dy dx \\ &\approx h^2 \sum_{i=1}^{N_x} \sum_{j=1}^{N_y} y_{i-\frac{1}{2}, j-\frac{1}{2}} \frac{1 + \phi_{i-\frac{1}{2}, j-\frac{1}{2}}}{2}. \end{aligned} \tag{64}$$

Figure 4   Variations of the quantity $2R_d^{eq}(\Delta p)^{eq}$ and the theoretical interfacial tension σ with the Weber number We with $Ca = 1$, $Cn = 0.15$, $Pe = 4 \times 10^3$, $N_L = 20$, $N_t = 80$
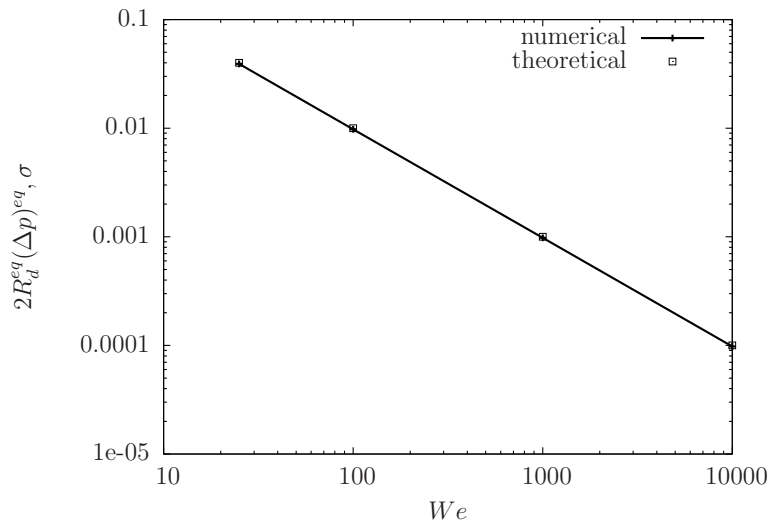
Figure 5   Evolutions of $\delta(\Delta p)$ (in percent) at different Cahn numbers $Cn = 0.2$, 0.1, 0.075, 0.05 (or interface widths $W = 6.4$, 3.2, 2.4, 1.6 (h)) with $Ca = 1$, $Re(= We) = 10^3$, $Pe = 2 \times 10^3$, $N_L = 32$, $N_t = 512$
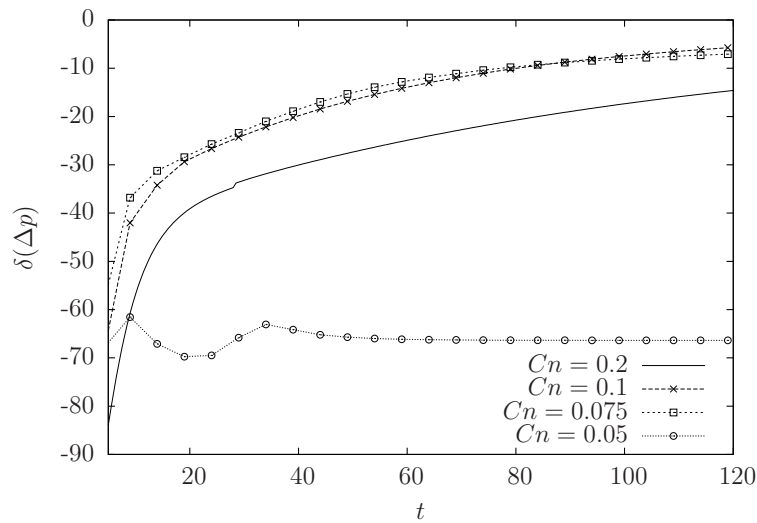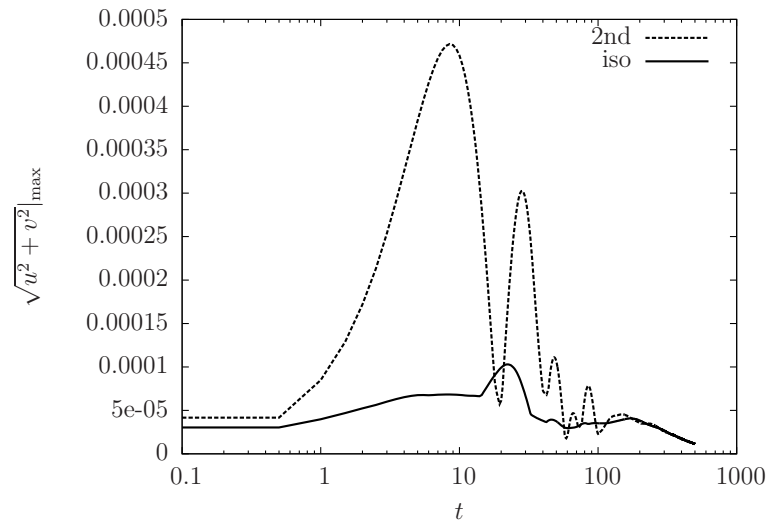

Figure 6   Comparison of the maximum velocity magnitude $\sqrt{u^2 + v^2}|_{\max}$'s evolution by the two schemes (`2nd` and `iso`) with $Re(= We) = 10^3$, $Ca = 1$, $Cn = 0.2$, $Pe = 4 \times 10^3$, $N_L = 20$, $N_t = 80$


Recall that y and x are actually the r and z coordinates of the cylindrical coordinate system. As emphasised by Ding et al. (2007), here the term *conservation* is not for a region enclosed by the interface ($\phi = 0$); instead, it is for the whole domain (i.e., in a global sense). Only when $Cn \to 0$, the mass *conservation* holds in both senses.

We study one specific problem with $Re(= We) = 10^3$. The interface width is fixed to be $W = 3.2$ (to maintain reasonable resolution of the ϕ−profile across the interface), and the Peclet number is fixed to be $Pe = 8 \times 10^3$. Other numerical parameters vary in different cases. For convenience, the cases are denoted as T1 (with $Cn = 0.2$, $N_L = 16$, $N_t = 48$), T2 (with $Cn = 0.1$, $N_L = 32$, $N_t = 96$), and T3 (with $Cn = 0.05$, $N_L = 64$, $N_t = 1024$). Figure 7 shows the change of V_d with time in $0 \le t \le 50$ for the three cases. It is seen that V_d almost remains constant in all cases. More careful quantitative examinations

reveal that the amplitudes of V_d's variation during this period are about 0.06%, 0.02%, and 0.006% of its initial value for T1, T2, and T3, respectively. Thus, the mass conservation is preserved fairly well (especially at lower Cn) although it is not as good as Ding et al. (2007), which claimed that it was preserved *to machine accuracy*. The possible reason is that the schemes employed in Ding et al. (2007) were conservative whereas the current ones are not. Nevertheless, as seen above, the violation of *mass conservation* is extremely small (only of order 10^{-4}). Besides, one finds from Figure 7 that V_d decreases (slightly) as Cn is reduced. This could be attributed to the reduced interfacial region at lower Cn. From the trend in V_d's change with Cn, it appears that a limit of V_d exists as $Cn \to 0$ (as expected from the convergence requirement).

Figure 7   Evolutions of V_d [defined in equation (64)] for three cases: T1 ($Cn = 0.2$), T2 ($Cn = 0.1$), and T3 ($Cn = 0.05$)
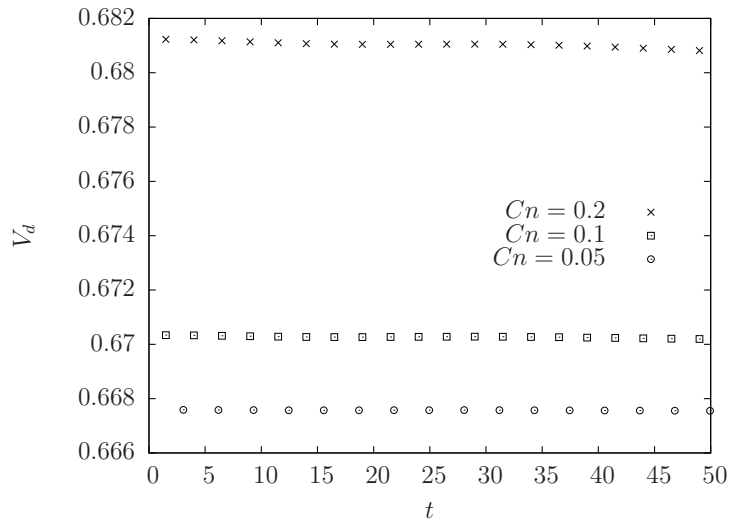
Note: The shared parameters are $Re(= We) = 10^3$ and $Pe = 8 \times 10^3$.

Figure 8   Evolutions of r_b for three cases, T1, T2 and T3, with different Cahn numbers
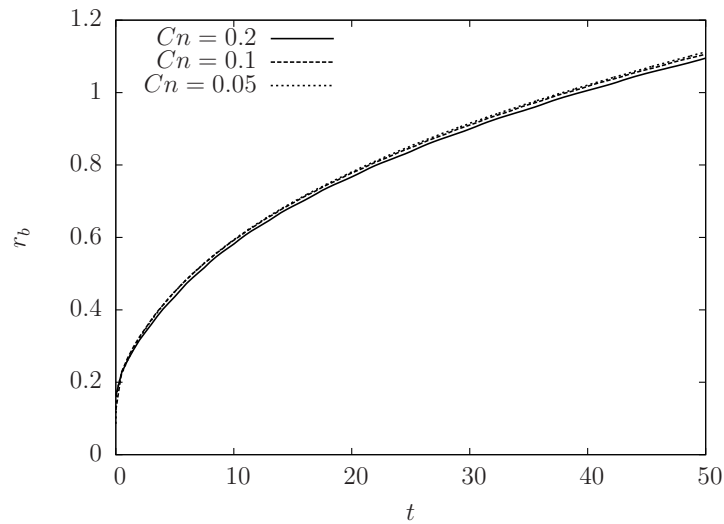
Note: The shared parameters are $Re(= We) = 10^3$ and $Pe = 8 \times 10^3$.

To check the convergence, the evolutions of r_b for the three cases with different Cahn numbers are plotted in Figure 8. Note that the study here is different from that in Section 3.3.2 because here the interface width is kept constant ($W = 3.2$). It is observed from Figure 8 that the difference in r_b between T2 ($Cn = 0.1$) and T3 ($Cn = 0.05$) is much smaller than that between T1 ($Cn = 0.2$) and T2 ($Cn = 0.1$). In fact the former is hard to see over a long time (e.g., $0 < t < 40$) from Figure 8. To balance the requirement of accuracy (which favours a Cn as small as possible) and the computational cost, we choose to use $Cn = 0.1$ for the studies below.

3.4.2   Effects of Re and comparison with other results

Before investigating the physical problem in detail, we want to mention a (minor) fix to the setup of this problem described above. In Figure 8, it is easy to find that $r_b(0) > 0$. However, equation (63) obviously predicts $r_b(0) = 0$. We suspect that it was probably due to the errors caused by the half-grid shift, the extrapolation to find r_b, as well as the finite interface width (for $Cn > 0$). Here one should notice the fact that significant topological change of the interface occurs at $t = 0$ (i.e., the drops start to coalescence) and this event is extremely sensitive to any numerical errors (in fact, there exists a singularity for this moment in sharp interface description). Through some

tests, we have found that to separate the drops a little bit could improve the results. In the following, we shift the drop a little along the axis and let $x_{c1} = 1 + \epsilon$ ($\epsilon \approx 1\%$, corresponding to a size less than $0.5h$), which adjusts $r_b(0)$ to be approximately zero.

We mainly investigate the drop coalescence under different Re (We) numbers: $Re(= We) = 1$, 10, 100, and 10^3. All cases share a few common parameters including $Cn = 0.1$, $Pe = 8 \times 10^3$, and $N_L = 32$, while N_t may differ in different cases. Figure 9 shows the variations of r_b with $\sqrt{t/Re_\sigma}$ for these cases (by different symbols), together with three lines predicted by equation (63) for $\alpha_g = 1.62$, 1.00, and 0.40, respectively. From Figure 9, it is seen that the scaling law $r_b \propto \sqrt{t}$ almost holds (roughly) in all the cases (when r_b is not too large), but the coefficients differ under different Re numbers. As reported previously, the scaling law agrees well with the experiments for r_b smaller than (about) 0.35 (Thoroddsen et al., 2005; Xing et al., 2007). Based on Figure 9, the coefficient seems to decrease as the Reynolds number is reduced. For instance, the coefficient for the case with $Re = 10^3$ seems to be slightly larger than 1.00 (note: focus on the early stage when $r_b < 0.35$), and that for the case with $Re = 1$ is slightly smaller than 0.40 .

In addition to the good agreement with the scaling law, the present results also agree well with the numerical results by the other method `MRT-LB-FD`. The details are not given here for this problem, but some careful comparisons will be provided for another problem next.

3.5 Study of contact angle, drop spreading/dewetting

In the final part there is a drop in contact with a solid wall with given contact angle (wettability). And we consider the spreading or dewetting of the drop on such a wall. Recall that the gravity is omitted in this work. Initially the drop sits on the left wall with a configuration corresponding to an initial contact angle of θ_i ($\theta_i = 90°$ or $120°$ in different problems). That is, the drop centre is $(x_c, y_c) = (0, 0)$ (for $\theta_i = 90°$) or $(0.5, 0)$ (for $\theta_i = 120°$). The actual wettability of the wall is specified by the equilibrium contact angle θ_w, which could differ from θ_i. When such a difference exists (i.e, $\theta_i \neq \theta_w$), the drop tends to spread (if $\theta_i > \theta_w$) or dewet (if $\theta_i < \theta_w$) towards a new configuration that would match θ_w. The domain size is $L_x \times L_y = 4 \times 4$. The physical parameters are $Re(= We) = 100$ ($Ca = 1$) except for Subsection 3.5.4 where $Re(= We) = 25$ ($Ca = 1$). The common numerical parameters are $Cn = 0.1$, $Pe = 8 \times 10^3$ ($S = 0.01118$), $N_L = 32$, and the temporal discretisation parameter is $N_t = 96$ except for Subsection 3.5.4 where $N_t = 128$. The interface width is $W = 3.2$ (as easily found from Cn and N_L). For this problem, we monitor two evolving variables: the drop *height* on the x−axis $H_x = H_x(t)$ and the drop *radius* on the (left) wall $R_y = R_y(t)$ (i.e., the radius of the circle on the wall formed by the contact line). By assuming that the drop shape is part of a sphere (which is a good approximation under negligible inertial effects), the (instantaneous) contact angle $\theta_{sf} = \theta_{sf}(t)$ may be deduced by rough shape-fitting just from these two quantities (Huang et al., 2011),

$$\theta_{sf} = \frac{180°}{\pi}\left(\pi - \arccos\left(\frac{1 - k_r^2}{1 + k_r^2}\right)\right), \quad (65)$$

where $k_r = R_y/H_x$ and θ_{sf} is in degree (°). To reduce the errors due to the half grid size shift, an improved method to find R_x^{eq} and R_y^{eq} was adopted to find R_y and H_x exactly located at the two lines, $x = 0$ and $y = 0$. Note that during the evolution, the inertial effects could become non-negligible, making the drop shape deform from a spherical one; besides, the interface near the contact line may be bent to some extent during the motion. Thus the rough shape-fitting may not be accurate enough during the motion but should suffice as an indicator after the drop reaches static equilibrium. It is noted that the problem setting in Section 3.4 of Huang et al. (2013) is different from the present one. In Huang et al. (2013), the initial drop centre was $(x_c, y_c) = (1, 0)$ (rendering an initial contact angle $\theta_i = 180°$), the static contact angle θ_w was fixed to be $90°$, and only spreading occurred. Besides, the case in Huang et al. (2013) has a (nominal) Reynolds number $Re = 20$ and some other numerical parameters also differ from those in the present work. For the slow drop spreading problem in Subsection 3.5.4, we also monitor the *apparent contact angle* θ_m and the contact line velocity V_{cl}. The *apparent contact angle* θ_m is obtained following the way described by Sui and Spelt (2013b,a). As shown by Sui and Spelt (2013b,a), the angle the interface makes with the wall (θ) is a function of the arclength away from the contact line along the interface (s), i.e., $\theta = \theta(s)$. It is known that the region near the contact line around the interface may be in general divided into three regions: the inner region, the intermediate region and the outer region based on the distance away from the contact line (Cox, 1986; Sui and Spelt, 2013b). For slow drop spreading, $\theta(s)$ is (almost) a linear function in the outer region (Sui and Spelt, 2013b), and it can be used to obtain the extrapolated angle at the contact line ($s = 0$). It is this angle that is taken as the *apparent contact angle* θ_m. Practically, we select the linear regime as $0.2s_{max} \leq s \leq s_{max}$ where s_{max} is the maximum of the arclength s (terminated at the axis) and we find the straight line through least squares fitting the points $(s, \theta(s))$ in this regime. Based on the recorded drop *radius* on the left wall $R_y(t)$, one can calculate the contact line velocity V_{cl} by using backward differentiation. For instance, $V_{cl}(t)$ at time t is found from,

$$V_{cl}(t) = \frac{1}{\Delta t}(R_y(t) - R_y(t - \Delta t)), \quad (66)$$

where Δt is the change in time and may take $k\delta_t$ with k being a positive integer (here $k = 1$). From the contact line velocity V_{cl}, another capillary number is obtained as $Ca_{cl} = \rho_c \nu V_{cl}/\sigma = V_{cl}/U_c$ (in other words, it is the contact line velocity V_{cl} measured in the characteristic velocity U_c).

Figure 9   Variations of r_b with $\sqrt{t/Re_\sigma}$ under different Re (We) numbers: $Re(=We) = 1,\ 10,\ 100,\ 10^3$
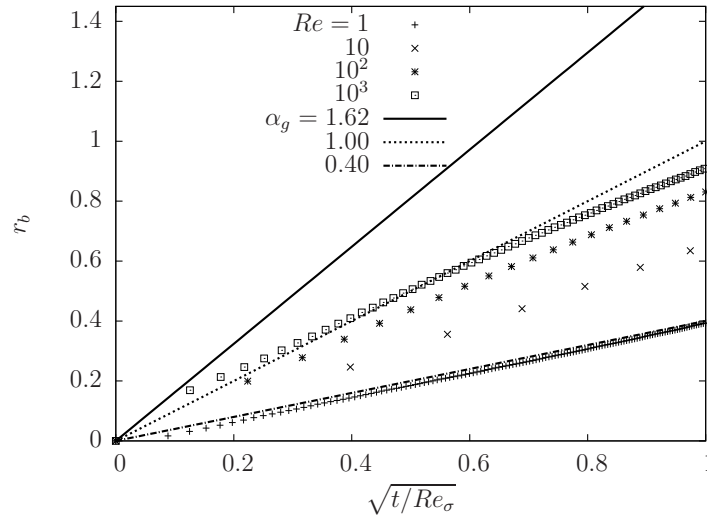
Note: The shared parameters are $Cn = 0.1$, $Pe = 8 \times 10^3$, and $N_L = 32$.

Figure 10   Evolutions of the difference between the contact angle θ_{sf} obtained by rough shape-fitting and the input contact angle θ_w, $\theta_{sf} - \theta_w$, under different θ_w $(30°, 60°, 120°,$ and $150°)$
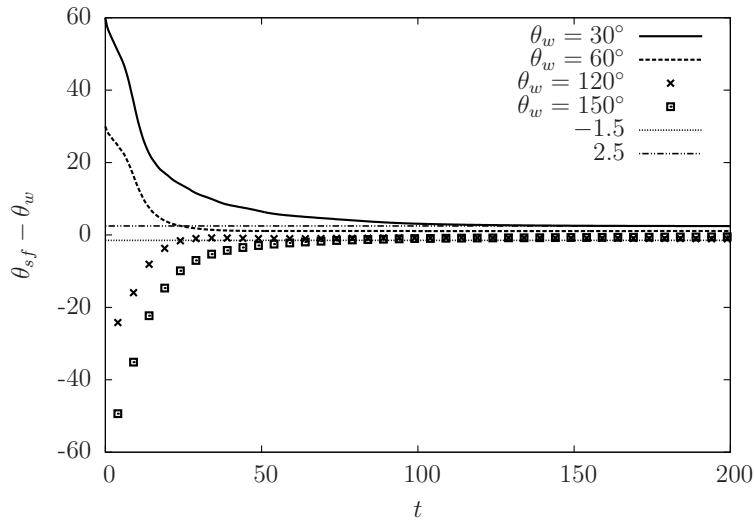
Before showing the results, we would like to highlight again the important issue of the convergence towards the sharp-interface limit (SIL), now for drop problems involving contact lines (though this work mainly focuses on proposing a numerical method using the VS formulation). Yue et al. (2010) systematically studied this issue and had some insightful findings and guidelines. One of them is that a SIL may be achieved by the phase-field model (using the CHE) through reducing Cn with other parameters fixed. The second is that the contact line dynamics is controlled by the diffusion length scale l_D [corresponding to the slip length l_s in some slip models to relieve the stress singularity near the contact line (Cox, 1986)]. Another is that to reach the SIL the interface width should satisfy $Cn_\varepsilon < 4S$. In what follows, we use $Cn = 0.1$ giving $Cn_\varepsilon = 0.035$, and

the parameter S is $S = 0.01118$. Therefore, the condition $Cn_\varepsilon < 4S$ can be satisfied. However, we note that this is a necessary condition, but not a sufficient one, to reach the SIL. As already discussed in Subsection 3.3.2, it is also required that $Cn \ll 1$, which is quite demanding when a uniform mesh is used (the pursuit of the SIL is beyond the scope of the present work).

3.5.1 Evolution of the contact angle θ_{sf} by rough shape-fitting

The contact angle θ_{sf} obtained by rough shape-fitting is investigated first. Figure 10 shows the evolutions of the difference between θ_{sf} and θ_w, $\theta_{sf} - \theta_w$, for several θ_w $(30°, 60°, 120°,$ and $150°)$. It is seen that for all

cases, $\theta_{sf} - \theta_w$ evolves towards zero. Finally, at $t = 200$ the deviations are quite small (between the two lines of $\theta_{sf} - \theta_w = -1.5°$ and $\theta_{sf} - \theta_w = 2.5°$, as seen from Figure 10). The maximum deviation (about 2.5°) was observed for $\theta_w = 30°$. These small deviations could be due to the errors in the measurement of R_y and H_x and/or in resolving the interface profile.

3.5.2 Comparison of the static contact angle

Next we compare the contact angle when the system is (almost) static after reaching equilibrium. This angle is denoted as θ_{sf}^{eq}. As there is (almost) no flow when reaching equilibrium, θ_{sf}^{eq} is considered as a reliable indicator to reflect the drop shape and contact angle. Figure 11 shows the equilibrium contact angles θ_{sf}^{eq}, as obtained numerically from equation (65) at $t = 200$, under different input values of θ_w (30°, 45°, 60°, 75°, 90°, 105°, 120°, 135°, and 150°). Also shown in Figure 11 is the straight line $\theta_{sf}^{eq} = \theta_w$ (which the points should fall on ideally). It is seen that the equilibrium contact angles from rough shape-fitting agree quite well with the input ones over a wide range. This shows (to some extent) the capability of the present method to handle drops with wetting on a wall.

3.5.3 Comparison between two methods: NSCH-VS(FD) vs. MRT-LB-FD

In this part, we compare the results of one selected case by the present method and the method in Huang et al. (2013) (MRT-LB-FD). Some good comparisons between them were already given in Huang et al. (2013) for a drop spreading problem with $\theta_i = 180°$, $\theta_w = 90°$, and $Re = 20$. Here we focus on a drop dewetting problem with the key parameters being $\theta_i = 90°$, $\theta_w = 135°$ at $Re = 100$. Note that a few more differences in other aspects (e.g., numerical parameters) exist between this work and Huang et al. (2013). Therefore, the new results given here would further verify the correctness of the two methods.

Figure 12 gives the evolutions of H_x and R_y [Figure 12(a) and 12(b)] and that of $\sqrt{u^2 + v^2}|_{max}$ [Figure 12(c)] from $t = 0$ to 100 by the current method, together with the corresponding evolutions by MRT-LB-FD for comparison. It is easy to see that the results by the two different methods agree quite well. As $\theta_w = 135°$ on the left wall, upon reaching static equilibrium, because of the conservation of mass the drop should (in theory) have a shape with $H_x = (1 + \cos\alpha)r = 1.38$ and $R_y = r\sin\alpha = 0.57$ where $\alpha = 180° - \theta_w = 45°$ and $r = [2/(2 + 3\cos\alpha - \cos^3\alpha)]^{1/3}$. These theoretical values are denoted by the horizontal lines in Figures 12(a) and 12(b). Under this set of parameters, it is observed in Figure 12(a) that H_x increases from 1.0 to a value slightly smaller than the theoretical one (1.38) during $0 < t < 40$ and then decreases slowly. From Figure 12(b), it is seen that R_y decreases from 1.0 to a value that is quite close to the theoretical one (0.57) during $0 < t < 40$ and, afterwards, it also decreases slightly. Further calculation

indicates that the deviation in H_x is less than 2.5% at $t = 100$. From Figure 12(c), it is seen that $\sqrt{u^2 + v^2}|_{max}$ shows two surges during $0 < t < 40$ and its maximum (i.e., U_{max}) occurs at the second surge with $U_{max} \approx 0.037$. After that period, it decays fast towards zero. The other Reynolds number Re_{max} can be estimated now to be $Re_{max} = U_{max}Re \approx 3.7$ (which is much, much smaller than Re).

Next, we compare the interface positions at selected times, during which significant changes occur, and also the flow field at one selected time with substantial macroscopic flow by the present method and by MRT-LB-FD. Figure 13 shows the interfaces (i.e., ,contour lines of $\phi = 0$) at $t = 0$, 10, 20, 30 [Figure 13(a)], and the flow field (shown through velocity vectors) at $t = 10$ [Figure 13(b)]. Note that in Figure 13(b) we zoom in the region near the vortex generated during the dewetting, which is close to the interface (thus only a part, instead of the whole domain, is shown). It is found that overall the two methods predict the interfaces to be located very close to each other at these selected moments. Besides, based on Figure 13(b), the flow fields at $t = 10$ calculated by them agree with each other well, though some small differences are observed in regions away from the drop. As mentioned in Huang et al. (2013), these small differences do not lead to substantial differences in the motion of the drop (as found from Figure 12).

3.5.4 Investigation of slow drop spreading

Lastly, we carry out some study of a drop that spreads on a homogeneous surface in the viscous regime. Unlike Huang et al. (2013), here we focus on the relation between the *apparent* contact angle θ_m and the contact line velocity-based capillary number Ca_{cl}. Cox (1986) analysed the spreading dynamics of an interface of immiscible liquids using matched asymptotic expansions and derived a formula between the apparent (macroscopic) contact angle θ_m and the wall (microscopic) contact angle θ_w (correct to order Ca_{cl}^0),

$$g(\theta_m) = g(\theta_w) + Ca_{cl}\ln(L_c/l_s), \qquad (67)$$

where l_s is the slip length usually much smaller than the macroscopic characteristic length L_c, and g is a complex function (also dependent on the viscosity ratio, see equations (3.21) and (7.11) in Cox (1986); we hide it for simplicity as we only consider cases with matched viscosity here). The quantity l_s/L_c is the slip length made dimensionless with L_c, and is denoted by λ below (following Ding et al., 2012; Sui and Spelt, 2013b). Sheng and Zhou (1992) provided an approximate relation between θ_m, θ_w and Ca_{cl} for two immiscible fluids with matched viscosity under the condition $|\cos\theta_m| < 0.6$ (note in Sheng and Zhou, 1992 an additional slip model dependent constant appears and it is assumed to be unity here),

$$\cos\theta_w - \cos\theta_m \simeq 5.63 Ca_{cl}\ln\lambda^{-1}. \qquad (68)$$

Figure 11 Comparison of the equilibrium contact angles θ_{sf}^{eq} obtained by rough shape-fitting with the input contact angle θ_w
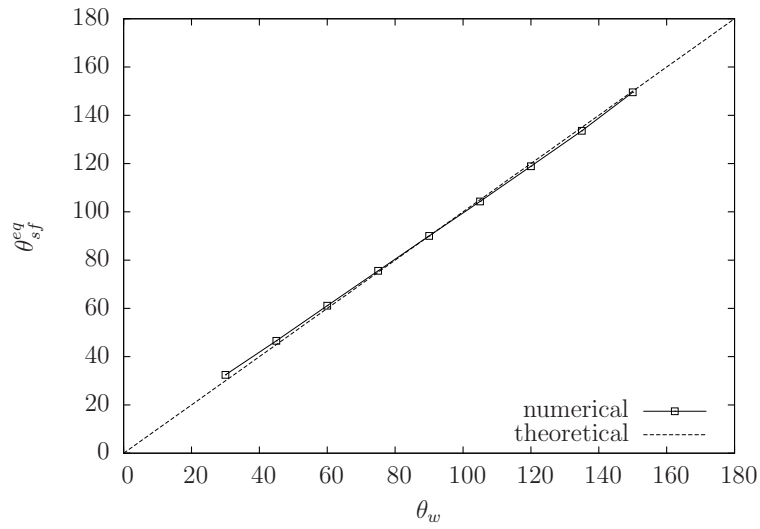

Figure 12 Comparison of the evolutions of (a) the drop height on the x−axis H_x, (b) the drop 'radius' on the (left) wall R_y, and (c) the maximum velocity magnitude $\sqrt{u^2 + v^2}|_{\max}$ by NSCH-VS(FD) and MRT-LB-FD with $Re(=We) = 100$, $Cn = 0.1$, $Pe = 8 \times 10^3$ ($S = 0.01118$), $N_L = 32$, $N_t = 96$, $\theta_w = 135°$, and $\theta_i = 90°$
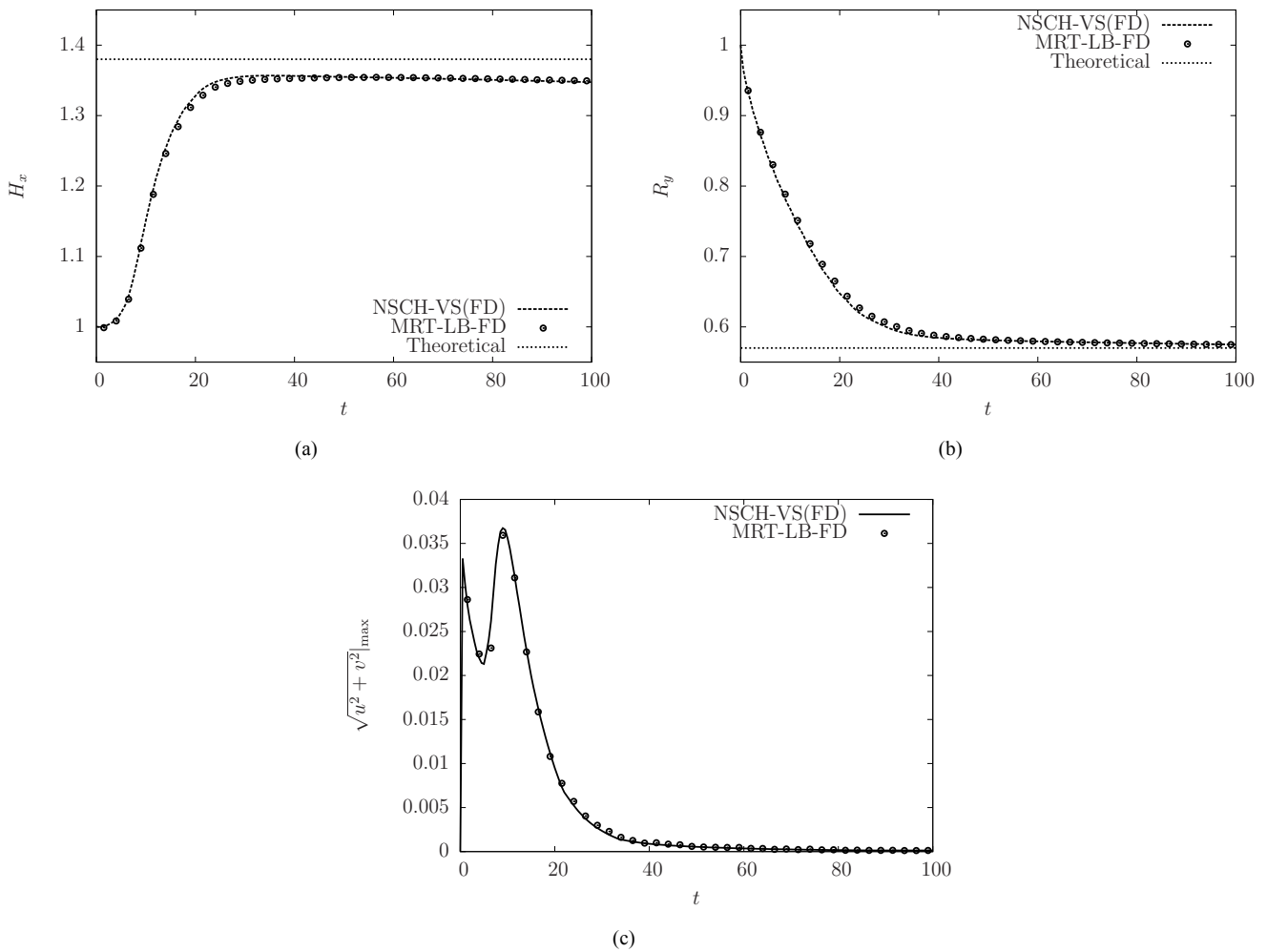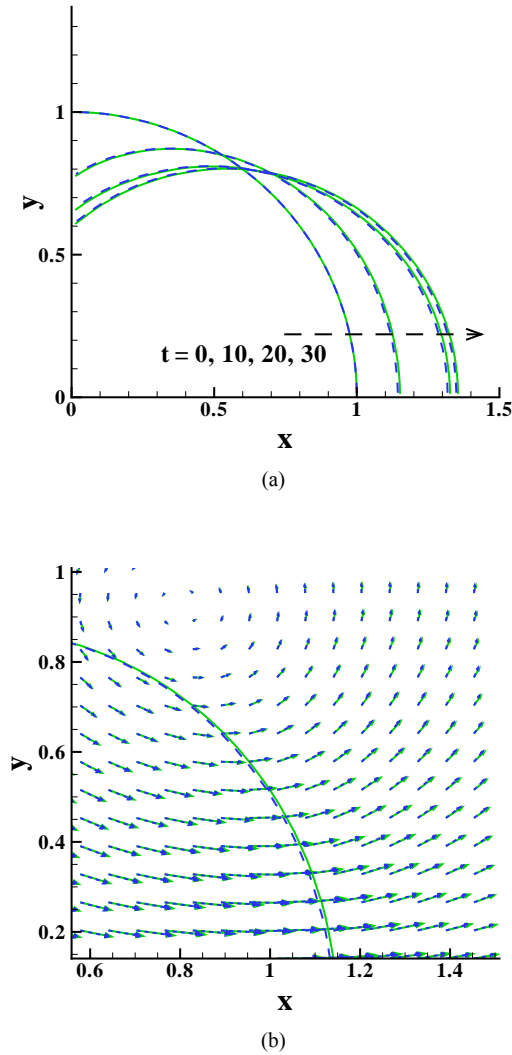

(a)

(b)

(c)

Figure 13 Comparison of (a) the interface positions at $t = 0,\ 10,\ 20,\ 30$ (b) the flow field (velocity vectors) at $t = 10$ by `NSCH-VS(FD)` (solid lines) and `MRT-LB-FD` (dashed lines) with $Re(= We) = 100$, $Cn = 0.1$, $Pe = 8 \times 10^3$ ($S = 0.01118$), $N_L = 32$, $N_t = 96$, $\theta_w = 135°$, and $\theta_i = 90°$ (see online version for colours)

(a)

(b)

We simulate one case with $Re(= We) = 25$ (giving an Ohnesorge number of $Oh = 0.2$). It is noted that the density ratio has almost no effect on the results for slow spreading (as reported in Sui and Spelt, 2013b). The initial velocity is zero, the initial contact angle is $\theta_i = 120°$ (with the centre of the drop $(x_c, y_c) = (0.5, 0)$) and the wall wettability is specified by $\theta_w = 60°$. The choice of these contact angles is to allow justified comparison with equation (68). The other parameters have been given before: $Cn = 0.1$, $Pe = 8 \times 10^3$ ($S = 0.01118$), $N_L = 32$, $N_t = 128$. Figure 14 shows the change of θ_m with Ca_{cl} during the spreading of the drop. The solid line is predicted by equation (68) with the dimensionless slip length set as $\lambda = 2.5S = 0.02795$ (giving $\ln \lambda^{-1} \approx 3.577$) and the symbols are from the present simulation. Here the determination of the slip length

($\lambda = 2.5S$) follows Yue et al. (2010). It is easy to see that the data points of the pair (θ_m, Ca_{cl}) obtained from the present simulation *roughly* fall near the line predicted by theory with a suitably chosen slip length. The seemingly small but finite deviations could be due to that the SIL has not been well attained because of the relatively large Cahn number ($Cn = 0.1$). Another observation from Figure 14 is that the $\theta_m - Ca_{cl}$ relation is not monotonic and shows some oscillations. Such oscillations could be caused by the capillary waves at the relatively large Cahn number.

Figure 14 Variation of the apparent contact angle θ_m with the contact line velocity-based capillary number Ca_{cl} during the spreading of a drop
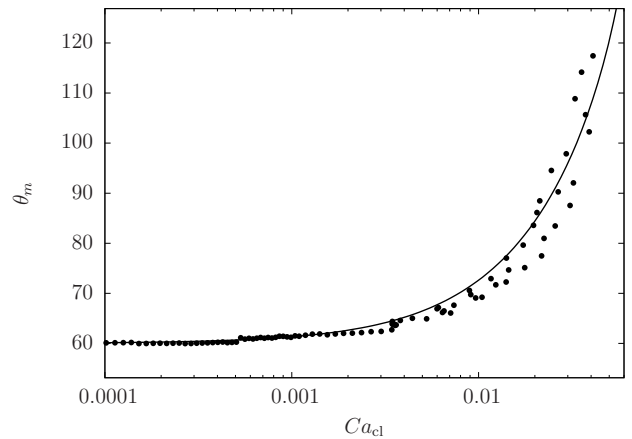
Notes: The solid line represents the prediction by equation (68) with the dimensionless slip length $\lambda = 2.5S$ (see Yue et al., 2010) and the symbols are from the present simulation. The physical parameters are $Re(= We) = 25$ ($Oh = 0.2$), $\theta_i = 120°$, $\theta_w = 60°$, and the numerical parameters are $Cn = 0.1$, $Pe = 8 \times 10^3$ ($S = 0.01118$), $N_L = 32$, $N_t = 128$.

4 Concluding remarks

To summarise, combining the VS formulation for hydrodynamics and the phase-field modelling of interface dynamics, we have presented systematically a numerical method for axisymmetric simulation of two-phase flows. It is 2nd-order accurate in space and 4th-order accurate in time. Applications of this new method for several benchmark problems have shown that it can deliver very good results that compare reasonably well with known theoretical results or other numerical ones. With the good features inherited from its two basic constituents, this method proves to be a useful tool for simulating axisymmetric multiphase problems. Future work may include the extension of this method for flows with different viscosities and/or densities, and for other types of flows (e.g., pressure driven flows). It may also be employed to explore in detail the dynamics of some interesting problems like drop coalescence.

Acknowledgements

References

Acar, R. (2009) 'Simulation of interface dynamics: a diffuse-interface model', *Visual Comput.*, Vol. 25, pp.101–115.

Anderson, P.D., Keestra, B.J. and Hulsen, M.A. (2006) 'On the streamfunction-vorticity formulation in sliding bi-period frames: application to bulk behavior for polymer blends', *J. Comput. Phys.*, Vol. 212, pp.268–287.

Anderson, D.M., McFadden, G.B. and Wheeler, A.A. (1998) 'Diffuse-interface methods in fluid mechanics', *Annu. Rev. Fluid Mech.*, Vol. 30, p.139.

Badalassi, V.E., Ceniceros, H.D. and Banerjee, S. (2003) 'Computation of multiphase systems with phase field models', *J. Comput. Phys.*, Vol. 190, pp.371–397.

Briant, A.J. and Yeomans, J.M. (2004) 'Lattice Boltzmann simulations of contact line motion. II. Binary fluids', *Phys. Rev. E*, Vol. 69, No. 3, p.031603.

Chang, Y.C., Hou, T.Y., Merriman, B. and Osher, S. (1996) 'A level set formulation of Eulerian interface capturing methods for incompressible fluid flows', *J. Comput. Phys.*, Vol. 124, p.449.

Chen, S. and Doolen, G.D. (1998) 'Lattice Boltzmann method for fluid flows', *Annu. Rev. Fluid Mech.*, Vol. 30, p.329.

Chen, S., Tolke, J., Geller, S. and Krafczyk, M. (2008a) 'Lattice Boltzmann model for incompressible axisymmetric flows', *Phys. Rev. E*, Vol. 78, No. 4, p.046703.

Chen, S., Tolke, J. and Krafczyk, M. (2008b) 'A new method for the numerical solution of vorticity-streamfunction formulations', *Comput. Methods Appl. Mech. Engrg.*, Vol. 198, pp.367–376.

Chorin, A.J. (1968) 'Numerical solution of the Navier-Stokes equations', *Mathematics of Computation*, Vol. 22, No. 104, pp.745–762.

Cox, R.G. (1986) 'The dynamics of the spreading of liquids on a solid surface. Part 1. viscous flow', *J. Fluid Mech.*, Vol. 168, pp.169–194.

Ding, H., Li, E.Q., Zhang, F.H., Sui, Y., Spelt, P.D.M. and Thoroddsen, S.T. (2012) 'Propagation of capillary waves and ejection of small droplets in rapid droplet spreading', *J. Fluid Mech.*, Vol. 697, pp.92–114.

Ding, H., Spelt, P.D.M. and Shu, C. (2007) 'Diffuse interface model for incompressible two-phase flows with large density ratios', *J. Comput. Phys.*, Vol. 226, pp.2078–2095.

Duchemin, L., Eggers, J. and Josserand, C. (2003) 'Inviscid coalescence of drops', *J. Fluid Mech.*, Vol. 487, pp.167–178.

E, W. and Liu, J-G. (1996) 'Vorticity boundary condition and related issues for finite difference schemes', *J. Comput. Phys.*, Vol. 124, pp.368–382.

Eggers, J., Lister, J.R. and Stone, H.A. (1999) 'Coalescence of liquid drops', *J. Fluid Mech.*, Vol. 401, p.293.

Ferziger, J.H. and Peric, M. (1999) *Computational Methods for Fluid Dynamics*, Springer, New York.

Huang, J.J., Shu, C. and Chew, Y.T. (2009) 'Mobility-dependent bifurcations in capillarity-driven two-phase fluid systems by using a lattice Boltzmann phase-field model', *Int. J. Numer. Meth. Fluids*, Vol. 60, pp.203–225.

Huang, J.J., Shu, C. and Chew, Y.T. (2011) 'Lattice Boltzmann study of bubble entrapment during droplet impact', *Int. J. Numer. Meth. Fluids*, Vol. 65, pp.655–682.

Huang, J-J., Huang, H., Shu, C., Chew, Y.T. and Wang, S-L. (2013) 'Hybrid multiple-relaxation-time lattice-Boltzmann finite-difference method for axisymmetric multiphase flows', *Journal of Physics A: Mathematical and Theoretical*, Vol. 46, No. 5, p.055501.

Jacqmin, D. (1999) 'Calculation of two-phase Navier-Stokes flows using phase-field modeling', *J. Comput. Phys.*, Vol. 155, p.96.

Jacqmin, D. (2000) 'Contact-line dynamics of a diffuse fluid interface', *J. Fluid Mech.*, Vol. 402, p.57.

Khatavkar, V.V., Anderson, P.D. and Meijer, H.E.H. (2007) 'Capillary spreading of a droplet in the partially wetting regime using a diffuse-interface model', *J. Fluid Mech.*, Vol. 572, p.367.

Lee, T. and Lin, C-L. (2005) 'A stable discretization of the lattice Boltzmann equation for simulation of incompressible two-phase flows at high density ratio', *J. Comput. Phys.*, Vol. 206, p.16.

Lee, T. and Liu, L. (2010) 'Lattice Boltzmann simulations of micron-scale drop impact on dry surfaces', *J. Comput. Phys.*, Vol. 229, pp.8045–8063.

Liu, H., Valocchi, A.J., Zhang, Y. and Kang, Q. (2013) 'Phase-field-based lattice boltzmann finite-difference model for simulating thermocapillary flows', *Phys. Rev. E*, Vol. 87, No. 4, p.013010.

Papatzacos, P. (2002) 'Macroscopic two-phase flow in porous media assuming the diffuse-interface model at pore level', *Transport Porous Med.*, Vol. 49, p.139.

Peyret, R. (2002) *Spectral Methods for Incompressible Viscous Flow*, Springer, New York.

Scardovelli, R. and Zaleski, S. (1999) 'Direct numerical simulation of free-surface and interfacial flow', *Annu. Rev. Fluid Mech.*, Vol. 31, p.567.

Sheng, P. and Zhou, M. (1992) 'Immiscible-fluid displacement: contact-line dynamics and the velocity-dependent capillary pressure', *Phys. Rev. A*, Vol. 45, No. 8, pp.5694–5708.

Stone, H.A., Stroock, A.D. and Ajdari, A. (2004) 'Engineering flows in small devices: microfluidics toward a lab-on-a-chip', *Annu. Rev. Fluid Mech.*, Vol. 36, p.381.

Sui, Y. and Spelt, P.D.M. (20113a) 'An efficient computational model for macroscale simulations of moving contact lines', *J. Comput. Phys.*, Vol. 242, pp.37–52.

Sui, Y. and Spelt, P.D.M. (20113b) 'Validation and modification of asymptotic analysis of slow and rapid droplet spreading by numerical simulation', *J. Fluid Mech.*, Vol. 715, pp.283–313.

Thoroddsen, S.T., Takehara, K. and Etoh, T.G. (2005) 'The coalescence speed of a pendent and a sessile drop', *J. Fluid Mech.*, Vol. 527, pp.85–114.

Tiribocchi, A., Stella, N., Gonnella, G. and Lamura, A. (2009) 'Hybrid lattice Boltzmann model for binary fluid mixtures', *Phys. Rev. E*, Vol. 80, No. 2, p.026701.

Unverdi, S.O. and Tryggvason, G. (1992) 'A front-tracking method for viscous, incompressible, multi-fluid flows', *J. Comput. Phys.*, Vol. 100, p.25.

Villanueva, W. and Amberg, G. (2006) 'Some generic capillary-driven flows. *Int. J. Multiphase Flow*, Vol. 32, pp.1072–1086.

Wu, M., Cubaud, T. and Ho, C-M. (2004) 'Scaling law in liquid drop coalescence driven by surface tension', *Phys. Fluids*, Vol. 16, No. 7, pp.L51–L54.

Xing, X.Q., Butler, D.L., Ng, S.H., Wang, Z., Danyluk, S. and Yang, C. (2007) 'Simulation of droplet formation and coalescence using lattice Boltzmann-based single-phase model', *Journal of Colloid and Interface Science*, Vol. 311, pp.609–618.

Yue, P., Zhou, C., Feng, J.J., Ollivier-Gooch, C.F. and Hu, H.H. (2006) 'Phase-field simulations of interfacial dynamics in viscoelastic fluids using finite elements with adaptive meshing', *J. Comput. Phys.*, Vol. 219, p.47.

Yue, P., Zhou, C. and Feng, J.J. (2007) 'Spontaneous shrinkage of drops and mass conservation in phase-field simulations', *J. Comput. Phys.*, Vol. 223, p.1.

Yue, P., Zhou, C. and Feng, J.J. (2010) 'Sharp-interface limit of the Cahn-Hilliard model for moving contact lines', *J. Fluid Mech.*, Vol. 645, pp.279–294.